LBNL-4103E

Pore-scale mechanisms of gas flow in tight sand reservoirs

Dmitriy Silin, Timothy J. Kneafsey, Jonathan B. Ajo-Franklin, and Peter Nico

Earth Sciences Division

Ernest Orlando Lawrence Berkeley National Laboratory

1 Cyclotron Road, MS 90R1116

Berkeley, CA

94720, USA

November 30, 2010

ABSTRACT: Tight gas sands are unconventional hydrocarbon energy resource storing large volume of natural gas. Microscopy and 3D imaging of reservoir samples at different scales and resolutions provide insights into the complex geometry of the pore space. Although the grains in tight sand samples do not significantly differ in size from conventional sandstones, the extremely dense grain packing makes the pore space tortuous, and the porosity is small. In some cases the inter-granular void space is presented by micron-scale slits, whose geometry requires imaging at submicron resolutions.

Maximal Inscribed Spheres computations simulate different scenarios of capillary-equilibrium two-phase fluid displacement. For tight sands, the simulations predict an unusually low wetting fluid saturation threshold, at which the non-wetting phase becomes disconnected. Flow simulations in combination with Maximal Inscribed Spheres computations evaluate relative permeability curves. The computations show that at the threshold saturation, when the nonwetting fluid becomes disconnected, the flow of both fluids is practically blocked. The nonwetting phase is immobile due to the disconnectedness, while the permeability to the wetting phase remains essentially equal to zero due to the pore space geometry. This observation explains the Permeability Jail, which was defined earlier by others. The gas is trapped by capillarity, and the brine is immobile due to the dynamic effects. At the same time, in drainage, simulations predict that the mobility of at least one of the fluids is greater than zero at all saturations.

A pore-scale model of gas condensate dropout predicts the rate to be proportional to the scalar product of the fluid velocity and pressure gradient. The narrowest constriction in the flow path is subject to the highest rate of condensation. The pore-scale model naturally upscales to the Panfilov's Darcy-scale model, which implies that the condensate dropout rate is proportional to the pressure gradient squared. Pressure gradient is the greatest near the matrix-fracture interface. The distinctive two-phase flow properties of tight sand imply that a small amount of gas condensate can seriously affect the recovery rate by blocking gas flow. Dry gas injection, pressure maintenance, or heating can help to preserve the mobility of gas phase. A small amount of water can increase the mobility of gas condensate.

1. Introduction: tight gas sand is an unconventional natural gas resource.

According to the United States Energy Information Administration (EIA) Energy outlook 2010 the contribution of natural gas in the United States Energy Portfolio was near 33 % in 2008. Starting from the mid-1980s, gas production increased. Unconventional gas resources accounted for 40 % of the entire gas production in 2008[1]. Over the past decade, production growth from unconventional resources outpaced the decline of production in the federal portion of the Gulf of Mexico (GOM), Figure 2. In projections into the future, it will grow to 46 % in 2035. Natural gas along with renewable sources of energy is expected to account for the majority of energy capacity additions by year 2035.

The United States Energy Information Administration (EIA) defines unconventional resources as *an umbrella term for oil and natural gas that is produced by means that do not meet the criteria for conventional production.* S. Holditch [49] states that the best definition of tight gas reservoir is *"a reservoir that cannot be produced at economic flow rates nor recover economic volumes of natural gas unless the well is stimulated by a large hydraulic fracture treatment or produced by use of a horizontal wellbore or multilateral wellbores."* Unconventional gas resources traditionally include tight gas sands, gas shales, and coal-bed methane. Although methane hydrates also represent a vast unconventional resource of natural gas [63, 64], there are significant uncertainties regarding how and when this resource may become an economically recoverable reserve [65, 74, 75, 103].

According to the EIA data, the major U.S. tight-sand gas fields are located in the mid-continent basins from Texas in the South to Montana and Dakotas in the North, plus in the Appalachian Basin to the east of Appalachian Mountains, Figure 3. Although the gas-shale production grows at a faster rate, the annual production volume is not expected to exceed the gas production in tight sands for substantial time. Apparently, tight gas reservoirs will remain a major energy resource for a long time.

The rock in tight gas reservoirs is characterized by permeability below millidarcy. Gas flow is usually associated with a network of natural or created fractures. Producing wells are typically stimulated by hydrofracturing. The high permeability of the fracture network is a consequence of the relative simplicity of the fracture geometry, rather than volume [11, 102, 105]. The main

[1]Report DOE/EIA-0383(2010), http: //www.eia.doe.gov/oiaf/aeo/lpnat_gas.html accessed on August 10 2010.

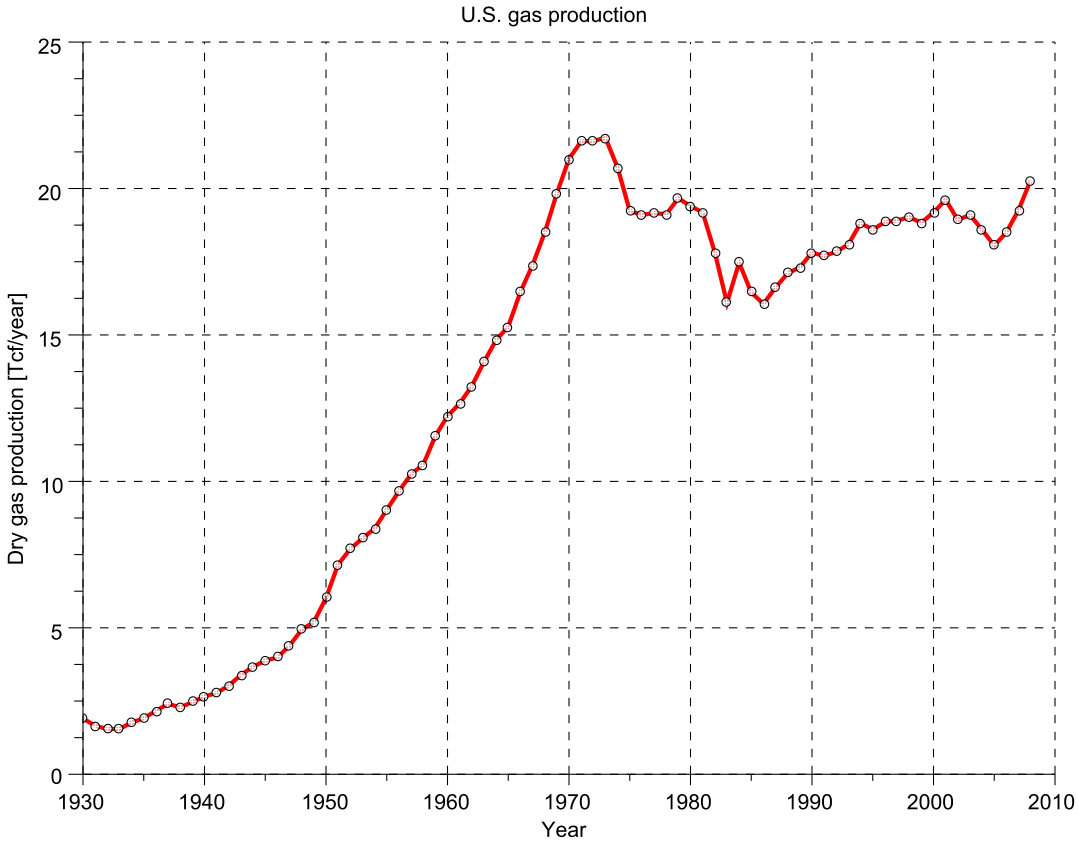

FIGURE 1. United States annual dry gas production between 1930 and 2008. Data: EIA.

part of the produced gas is extracted from the rock matrix. To be recovered, the gas must be released into the fracture network and then transported to the producing well. Consequently, flow in the matrix and matrix-fracture interaction play crucial roles in ultimate gas recovery.

Natural gas is a complex multicomponent hydrocarbon. In a multicomponent system, some fractions can dropout as liquid at depleting pressure. This phenomenon is called retrograde condensation [34, 56]. The sharp contrast between matrix and fracture permeability may create a steep pressure gradient at the interfaces between the matrix blocks and the fractures. This pressure gradient can stimulate gas condensate dropout. The presence of gas condensate makes the flow two-phase. In low-permeability rock, a relatively small amount of condensate can block the pore channels and significantly hinder gas flow.

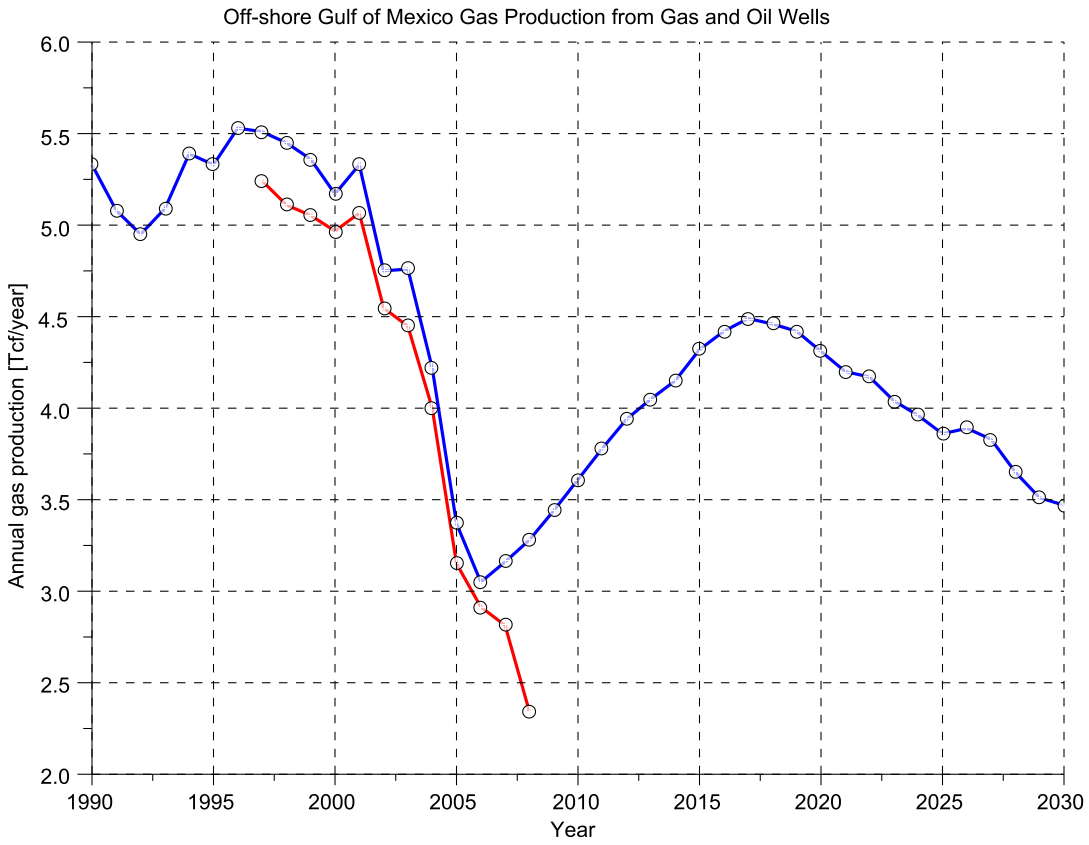

FIGURE 2. Offshore gas production in Tcf/year from the federal portion of GOM. The blue line shows the off-shore gas production projections in the 2008 Annual Energy Outlook. The noticeable production decline is offset by the unconventional natural gas production. Data: EIA.

Although the radius of influence of a gas well may be of the order of hundreds of meters, the gas to be produced is stored in pores whose size can be of the order of microns. A zillion processes developing in the pores sum up and eventually determine the efficiency and success of the recovery operations. The principal objective of this study is to gain insights and better understanding of the pore-scale mechanisms of gas flow in low-permeability rock and its impact on gas recovery. Technically, our approach is to investigate the geometry of the pore space in tight sands and its impact on permeability and two-phase properties of the rock. Seeing often provides a clue to understanding. A major effort within present work is application of x-ray computed tomography (CT) for three-dimensional imaging of the pore space of reservoir samples

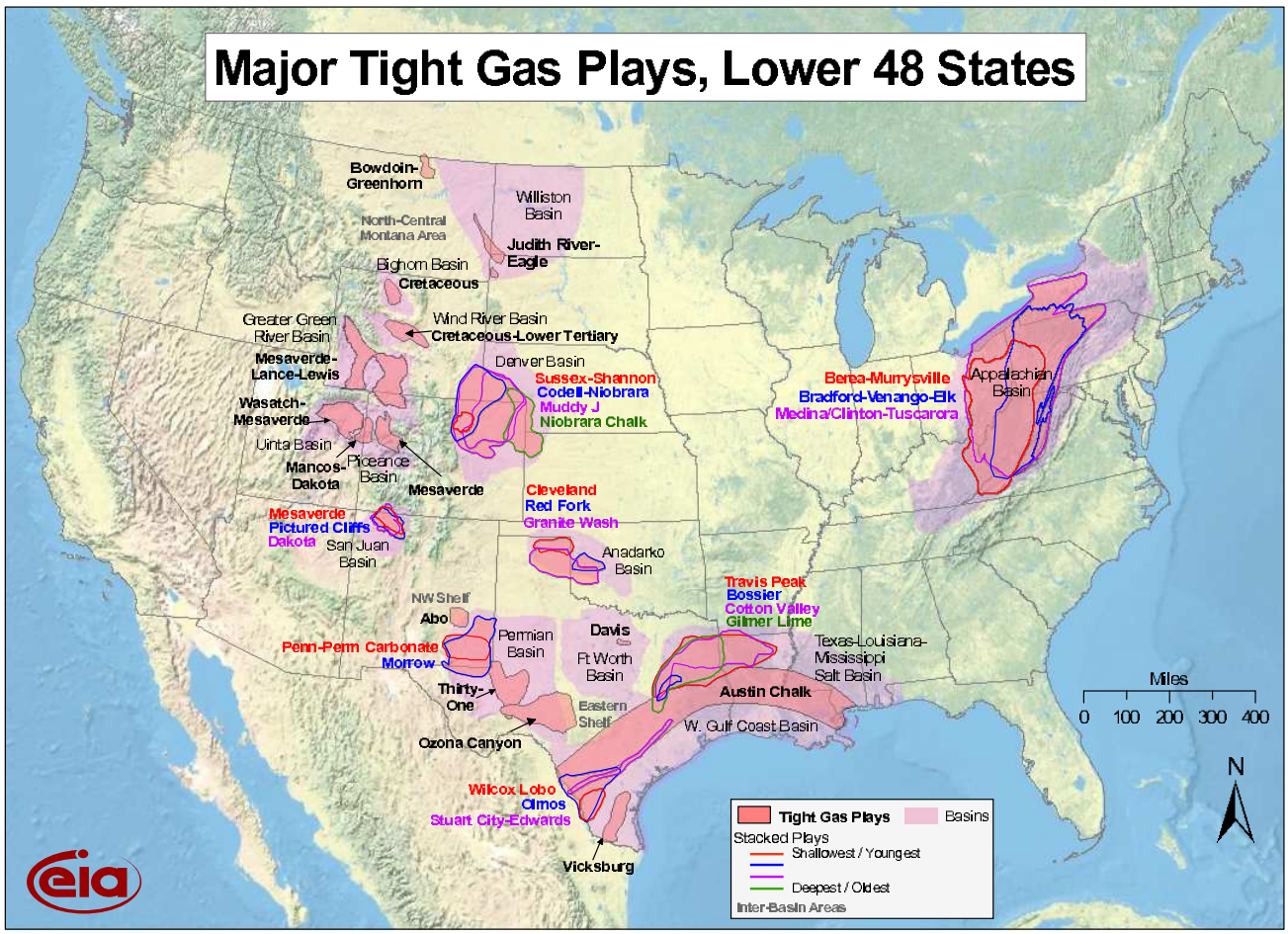

Source: Energy Information Administration based on data from various published studies
Updated June 6, 2010

FIGURE 3. The EIA map of the major U.S. tight sand gas plays updated in 2010.

at different scales. Maximal Inscribed Spheres computer simulations (MIS, [95, 97, 98, 101]) use segmented CT images of rock samples as input data to evaluate capillary-equilibrium two-phase fluid distribution. The simulations predict that a relatively small amount of the wetting liquid, whether it is brine or gas condensate, may trap gas by making it disconnected. We use MIS calculations in combination with flow simulations to estimate the relative permeability curves and give a pore-scale interpretation of the Permeability Jail phenomenon [23, 93] as interaction of capillary and dynamic forces. We employ simple equilibrium thermodynamics to develop a pore-scale model of retrograde condensation in gas flow. The model suggests that the condensate dropout is concentrated in narrow throats connecting clusters of larger pores. Upscaling from pore to Darcy length scale transforms this model into Panfilov's model [84, 85], according to which the rate of condensate dropout is proportional to the pressure gradient squared.

The report is organized as follows. First, we overview application of the X-ray CT technique to imaging tight-sand rock samples. We will discuss the segmentation for extracting a digital image of the pore space. Then we describe the method of maximal inscribed spheres for simulating two-phase fluid distribution and estimating capillary pressure curves. This discussion is followed up by development of a finite-difference flow simulator for estimating the absolute permeability. A combination of this simulator with MIS fluid distribution is used to estimate the relative permeability curves. Finally, we summarize the findings and formulate conclusions. The study focuses on five samples named, for brevity, sample 1, 2, 3, 4, and 5. Figures 9 (b) and 10 below show micro-CT cross-sections of these samples.

2. Experimental: X-ray computed microtomography

2.1. **Low-resolution tomography.** Samples of tight sandstone were photographed and then scanned using a modified Siemens Somatom HiQ medical computed tomography (CT) scanner providing 194 micron × 194 micron × 1000 micron voxels (rectangular parallelepiped-shaped volume elements over which the density is computed). Homogeneous samples of light element materials having known density were also scanned to provide a density calibration curve. Photographs and cross sections from the resulting 3-D density maps are presented in Figures 4–6. Three cross sectional images are shown in each of the Figures (a)–(c). The samples will be named with numbers 1, 2, and 3. These cross sections were selected because they show specific characteristics of the sample.

An artifact of using a polychromatic x-ray source is beam hardening [94]. Lower energy (softer) x-rays are more strongly absorbed in the outer regions of the core giving it a brighter (higher density) appearance. This artifact is visible in all the CT images shown here, and most strongly seen in smaller diameter cores. The studies cores were large enough so that only the inner portions of the core images, which were free of the beam hardening effect, were analyzed.

The most obvious visual features in Sample 1 (Figure 4) are non-connected dark lenses in the sandstone. The CT scanning shows these features as having a higher density than the surrounding rock. The rock appears to have larger-scale heterogeneity than in Sample 2 below, with a layer of higher density material cross cutting the sample (Figure 5 (c)). This layer appears to be composed of a higher spatial density of the higher density lenses. The density of these features is close to that of quartz, thus very low porosity. The remainder of the rock has an

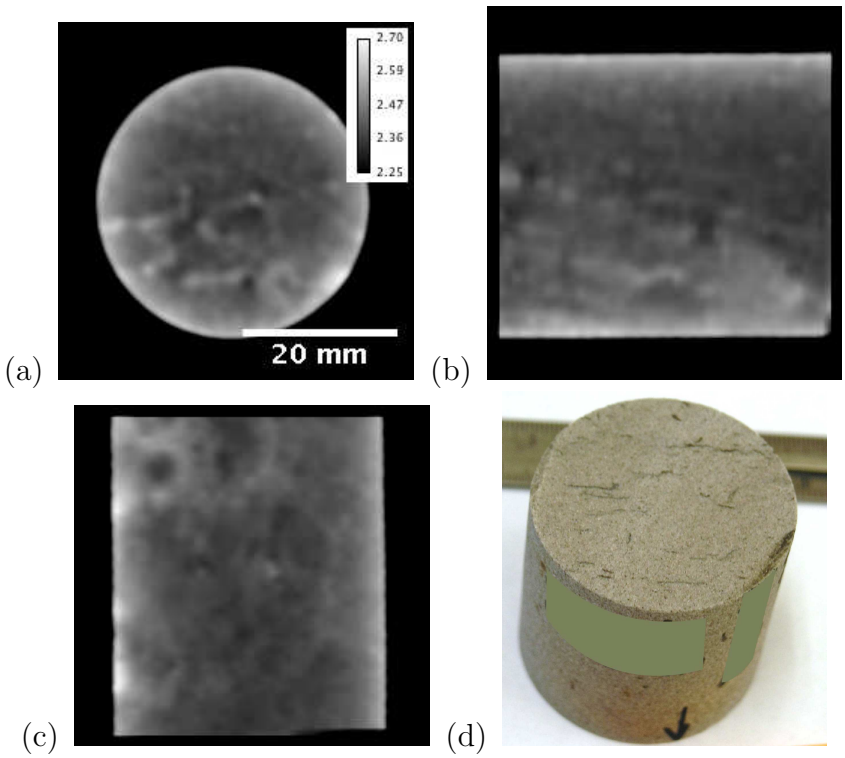

FIGURE 4. X-ray CT images of Sample 1 (a) axial cross section, (b) cross section along vertical central plane of (a), and (c) cross section along horizontal central cross section of (a), (d) photograph of core.

estimated porosity of about 8 %. Small unconnected higher porosity regions ($\sim$ 10 %) are also observed in the CT scans.

Figure 5 presents results from Sample 2. This sample is a dense, well-cemented sandstone. From the photograph, laminations in the rock are visible. The CT scanning also shows laminations with relatively large density differences between layers. Contrasting layers have variability in density from about 2.4 to 2.6 g/cm^3. Comparing this to the density of quartz (2.65 g/cm^3) gives a porosity estimate of 2 % to 9.5 % in these contrasting layers.

Images from Sample 3 are shown in Figure 6. This sandstone is composed of coarser grains than the other two samples, is laminated on approximately the same spatial scale as Sample 1, and contains numerous high-density grains distributed throughout the sample. This sandstone is probably composed of grains that are higher in density than quartz, as the bulk density exceeds that of quartz.

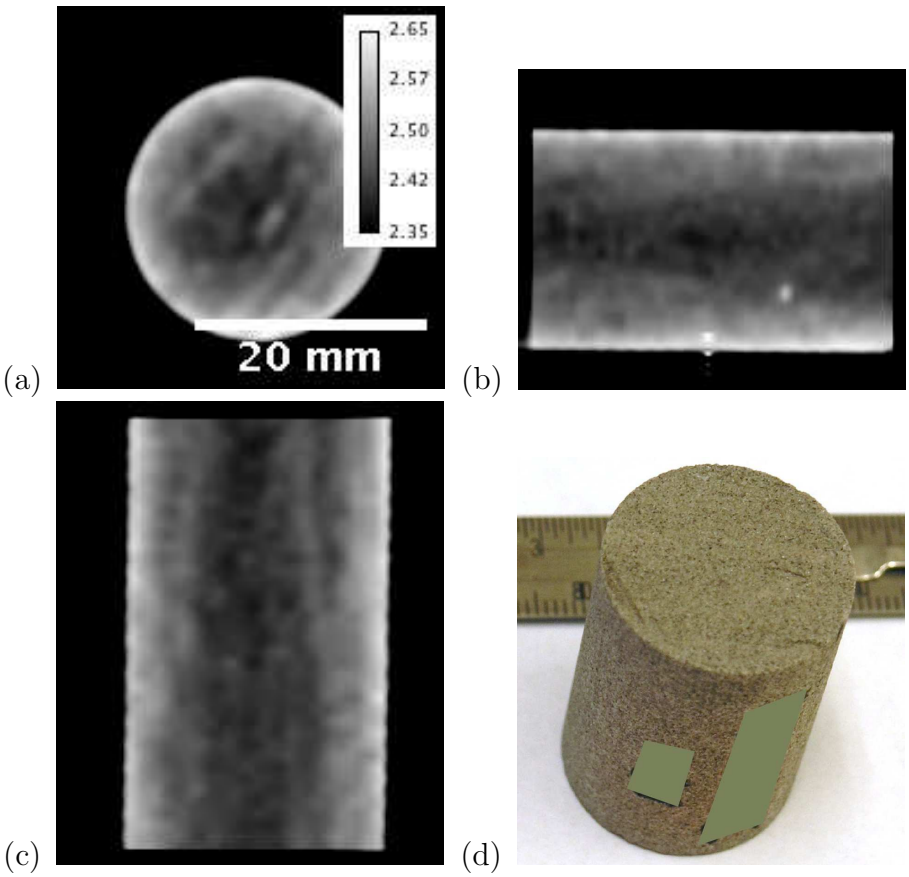

FIGURE 5. X-ray CT images of Sample 2: (a) axial cross section, (b) cross section along vertical central plane of (a), and (c) cross section along horizontal central cross section of (a), (d) photograph of core.

2.2. **X-ray microtomography at the ALS.** X-ray CT imaging is widely used in medicine, but it also has become a useful tool in the studies of the 3D pore stricture of natural rocks [7, 24–26, 99]. The LBNL x-ray micro-tomography facility is based at beamline 8.3.2 at the Advanced Light Source (ALS). The setup is similar to the standard setup for this technique developed in the 1990's [57]. The x-rays are produced from a superbend magnet source and pass through a monochromator comprised of two multilayer mirrors, which can be altered in angle to select the required x-ray energy. X-rays of energy 8 KeV to 45 KeV are available. X-ray energy was adjusted to a given total attenuation of the sample of $\sim$ 1500 to 2000 arbitrary absorption units. The samples were mounted on an air bearing stage that can be adjusted in three dimensions relative to the x-ray beam. The x-rays transmitted through the sample then interacted with a $CdWO_4$ single crystal scintillator that fluoresces the shadowgram x-ray image as visible light. This image was then magnified through a choice of microscope objectives and relayed onto a

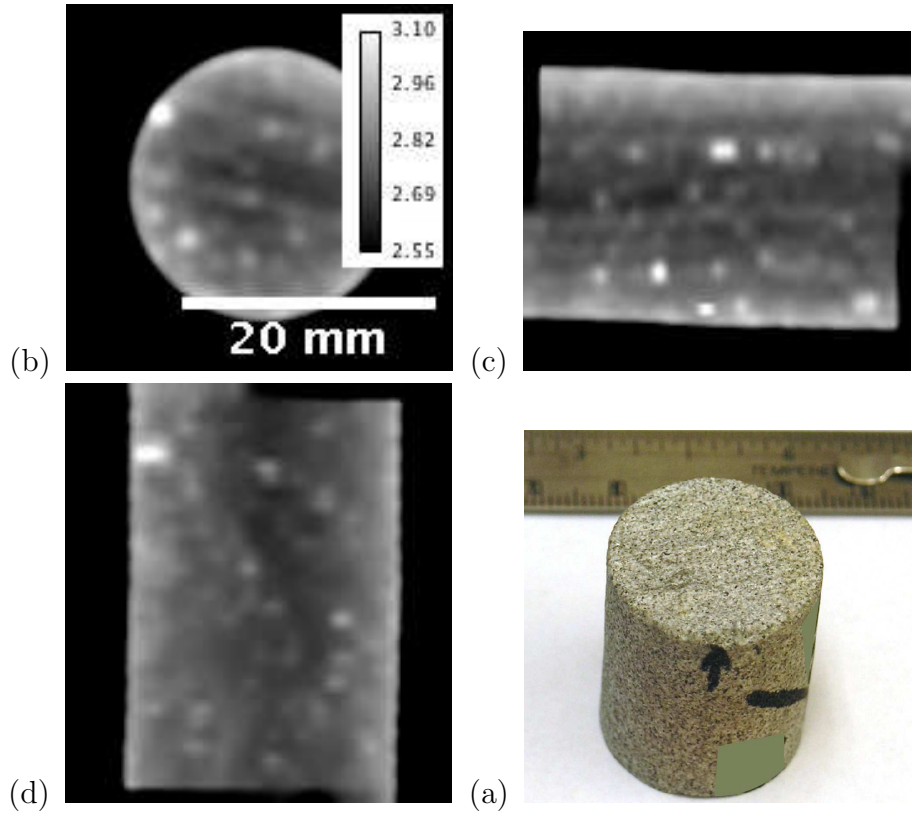

FIGURE 6. X-ray CT images of Sample 3: (a) axial cross section, (b) cross section along vertical central plane of (a), and (c) cross section along horizontal central cross section of (a), (d) photograph of core.

4008×2672 pixel CCD camera (Cooke PCO 4000). The CCD pixel size is 9 μm, thus with a 2×, 5×, or 10× objective a pixel size of 4.5 μm, 1.8 μm, or 0.9 μm, respectively, at the sample can be mapped onto the ccd. Due to the ccd's fixed field of view, increases in objective magnification require a proportional decrease in physical size of the sample. The maximum sample diameter is $\sim$ 15 mm, $\sim$ 6 mm, and $\sim$ 3 mm for the 2×, 5×, and 10× objective, respectively. The samples were rotated in the x-ray beam from angles 0 to 180 degrees with images collected at the desired angular increment. The most common angular increment was 0.125 degrees, 1441 images, as this was shown to be a good compromise point between the greater reconstructed image quality derived from collecting a greater number of raw images and scan time. Single image exposure times ranged from a minimum of several hundred microseconds to several seconds. Multiple images at a single angular location were averaged to avoid detector saturation during longer exposure times. The raw data were reconstructed using the commercial software package Octopus [32] using a filtered back projection algorithm.

2.3. **SEM imaging of microporosity.** In comparison to x-ray micro CT, scanning electron microscopy (SEM) is a traditional high-resolution imaging technique which uses the interaction of a focused electron beam with the sample to image features as small as 2–3 nm. Unlike micro CT, SEM is only capable of imaging sample surfaces but allows access to smaller length scales with the addition of compositional information from secondary spectroscopy measurements (e.g. EDS, WDS, EELS, EBSD)[2]. We utilize SEM in a supporting role to understand pore scale clay distribution and plan to incorporate EDS measurements in the future to resolve phase identification questions. We carried out our high resolution work using a field-emission SEM (Hitachi S-5000); for more routine tasks we used a smaller tabletop electron microscope (Hitachi TM-1000).

Figure 7 shows a series of backscattered electron (BSE) images acquired for a small tight sandstone core depicting two different types of clay accumulation within the pores. Panel 4A shows typical stacks of pseudo-hexagonal kaolinite platelets occupying the space between two quartz grains while 4B shows less ordered montmorillonite distribution in another pore throat. Textural differences as shown in these image are difficult to resolve in micro CT imagery; the kaolinite platelets have characteristic lateral dimensions of 3–4 microns with inter-platelet spacings of less than a micron in many cases making resolution using micro CT problematic. The high surface area and variety of smaller pores present in the clays occupying spaces between sand grains will have significant impact on both permeability and gas adsorption. Unfortunately, without the use of focused ion beam methods to sequentially remove layers of the core, images of this type are limited to views of the rock surface which is in many cases contaminated by the coring and polishing process.

Figure 8 shows a comparison of a micro CT slice and an surface SEM image for the same core. From a flow modeling perspective, a micro CT slice (1.8 microns thick) provides a better planar cross-section. However, the contrast limitations in micro CT make segmenting quartz grains from clay fill difficult if only intensity is used in the analysis process. While SEM is limited to a surface image, the texture of the filling clay is readily apparent.

[2]EDS stands for energy-dispersive X-ray spectroscopy, WDS stands for wavelength dispersive spectroscopy, EELS stands for electron energy loss spectroscopy, and EBSD stands for Electron Back Scatter Diffraction.

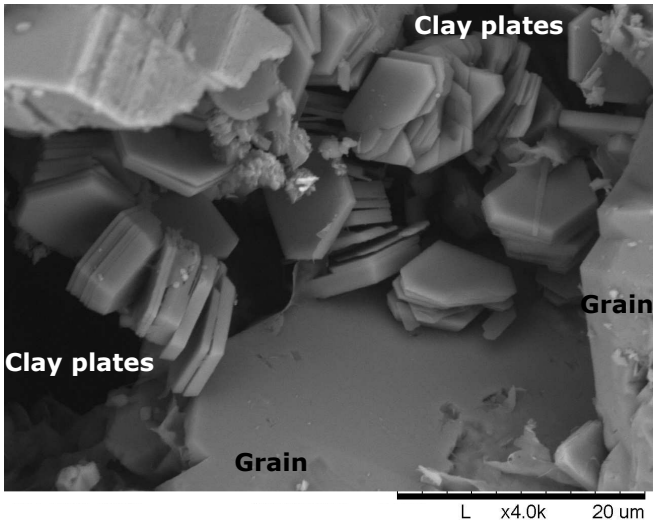

(A)

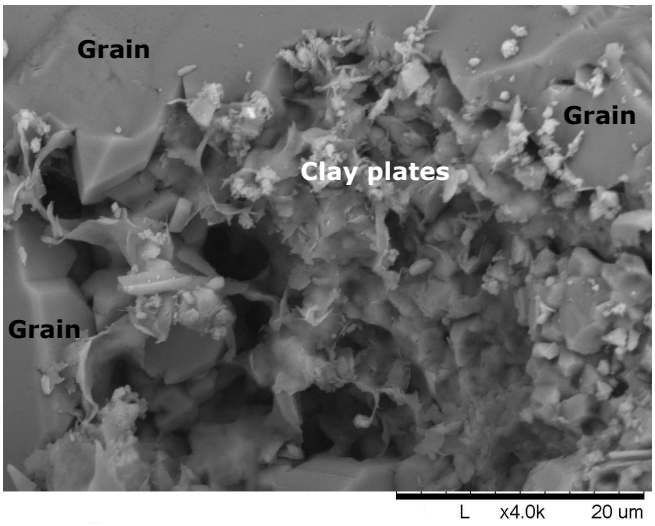

(B)

FIGURE 7. SEM 4000× magnification images show different types of clay plates contribute to the microporosity of the sample: kaolinite (A) and montmorillonite (B).

3. A model of two-phase fluid distribution in tight sands

3.1. **Tight sands micro CT images.** The term "tight sand" is not rigorously defined. One of the definitions is sands requiring well stimulation for gas production. In grain-scale level, tight sands are usually dense packing of small grains. Figure 9 (b) shows a cross-sections of a CT image of tight-sand sample in comparison to a conventional sandstone sample, Figure 9 (a)[3].

[3]The conventional sandstone image is courtesy of Dr. Liviu Tomutsa of Lawrence Berkeley National Laboratory.

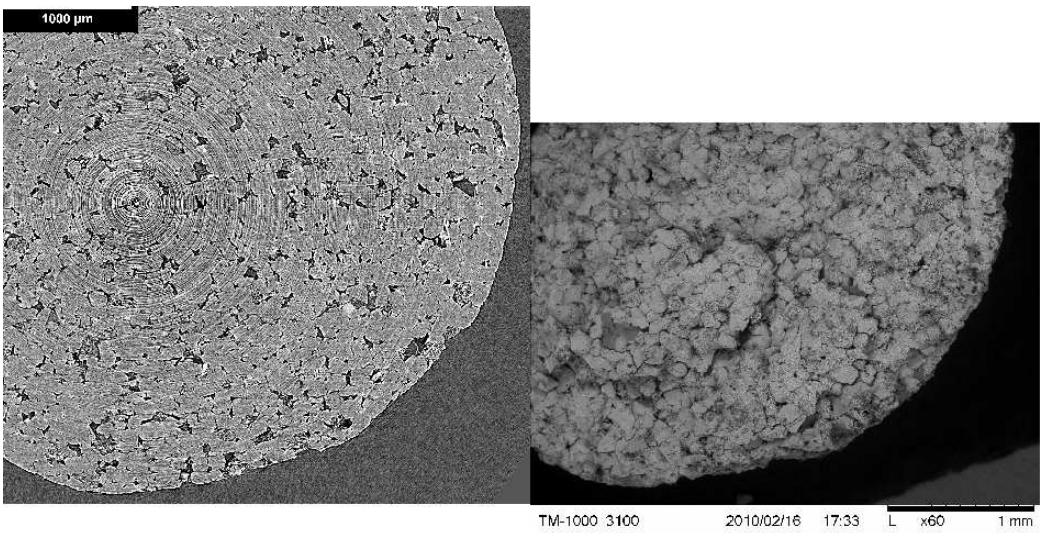

FIGURE 8. A micro CT reconstruction, on the left, accurately reproduces a planar cross-section of a sample, whereas a SEM image, on the right displays the rough surface of the sample.

(a) 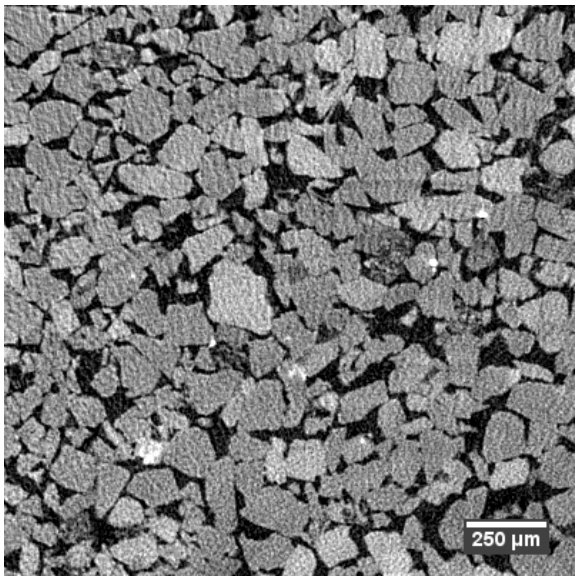

(b) 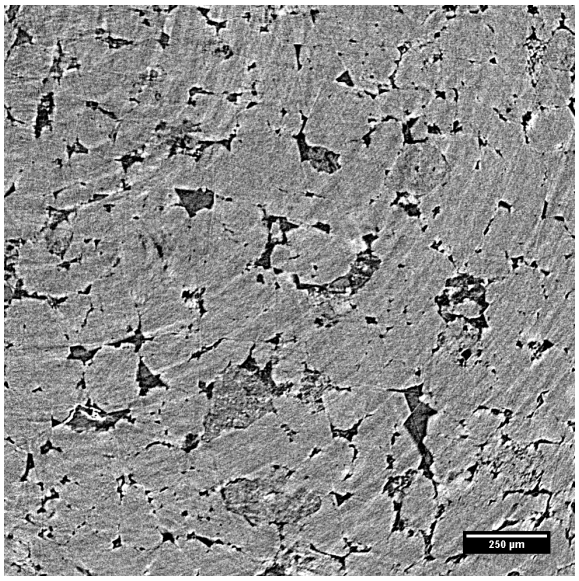

FIGURE 9. Two-dimensional cross-sections of micro-CT images of conventional (a) and tight sand (b) samples at resolutions of 4.4 and 1.8 microns, respectively.

Note that even though the grain sizes and shapes do not differ dramatically, the porosity of a tight-sand sample is dramatically smaller than that of the conventional sand.

The small porosity creates difficulties in image reconstruction and segmentation. Additionally, the pores are frequently filled with clay particles whose dimensions are much smaller than those of the grains, see Figure 7. The image of tight sand sample in Figure 9 (b) (named "sample 1"

below) should be compared with images of the other samples, named samples 2,3,4, and 5, Figure 10. The densely packed grains in samples 3 and 4 leave almost no room for porosity. The lighter color in the images indicate a higher density of the material. The quartz grains are in dark-gray color. The images have been acquired at the Advanced Light Source x-ray microtomography facility at different time. The facility upgrades resulted in higher quality and higher resolution image of sample 3.

The concentric rings noticeable in the gray-scale images, Figures 9 (b) and 10, are computed tomography image reconstruction artifacts [59]. Segmentation and cluster-search cleanup described in Section 3.3 below filter out these artifacts.

Figure 11 shows micrographs of samples 1 and 2. The shapes of grains and pores are consistent with the cross-sections of micro-CT images. Figure 12 shows micrographs of samples 4 and 5. Both images display complex pore geometries. Note an unusual structure resembling a small droplet pending at the tip of a stem in the right-hand picture.

Figure 13 shows a three-dimensional reconstruction of a tight sand sample. The lighter color denotes pores, whereas grains are dark-gray. The size of the cube is approximately 0.92 mm.

3.2. **Image segmentation.** To run simulations on a micro-CT image the voxels have to be divided into either pore or solid. Processing the image with a segmentation algorithm produces a binary array where each voxel is assigned a value indicating whether it is pore or solid. This operation is always ambiguous. Some voxels entirely fit into the void space, and some are entirely in the solid phase. However, due to the finite voxel size and the complexity of the pore space geometry, a number of voxels are neither entirely in the pores nor entirely in the solid. The presence of noise in the reconstructed image can further complicate the decision of assigning the appropriate voxel value. A comparison among a number of segmentation algorithms in [52, 92] has not defined a clear winner. Apparently, each particular application may require an individual approach.

For high-porosity samples, the histogram of intensities of a CT image usually has two well-defined peaks corresponding to the pores and solid. Thresholding the pore-solid intensity values at the trough between the peaks in the histogram produces reasonable segmentation [101, Figure 4]. However, the porosity in tight-sands is small, and such a minimum may not be easy to find, Figure 14.

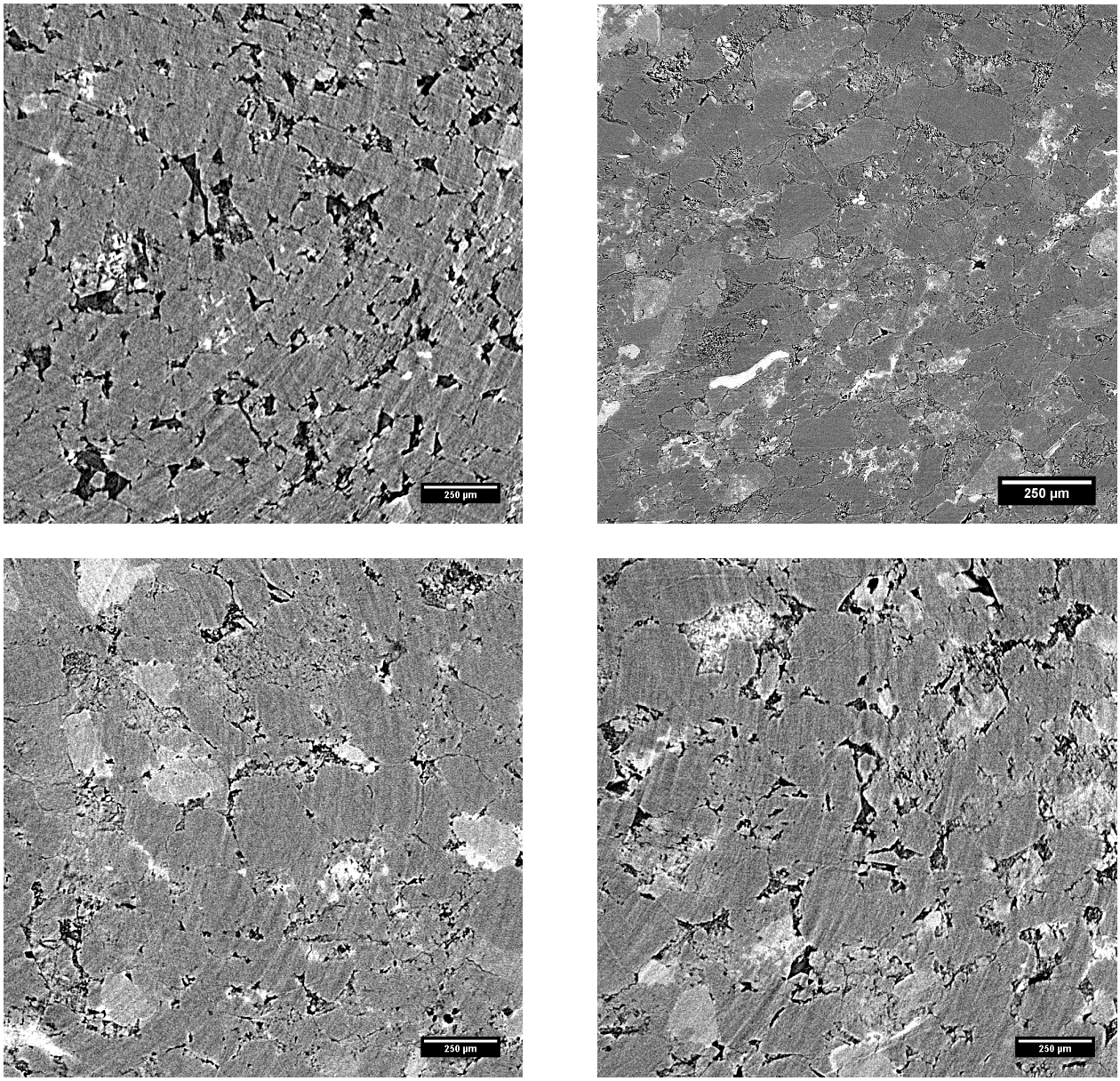

FIGURE 10. Two-dimensional cross-sections of micro-CT images of tight sand samples. Voxel size is 1.8 microns, except the top right image, where the voxel size is 0.9 micron. The samples are numbered 2–5 row-wise, starting from the top left image.

It turns out that the contrast of the CT image is sufficient for assigning the threshold intensity in a simple way. We illustrate the idea on a cross-section of CT reconstruction of sample 1. The

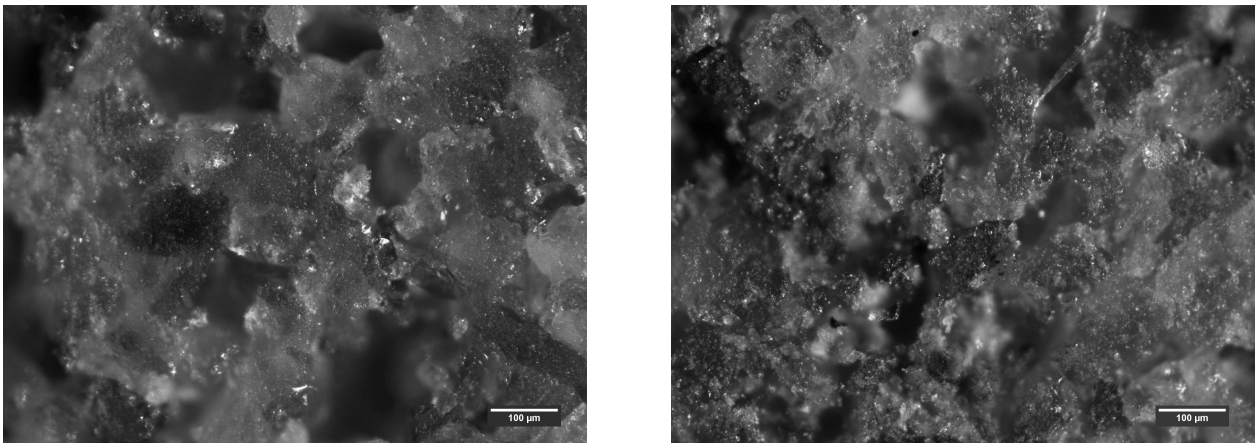

FIGURE 11. Micrographs of tight sand samples 1 and 2.

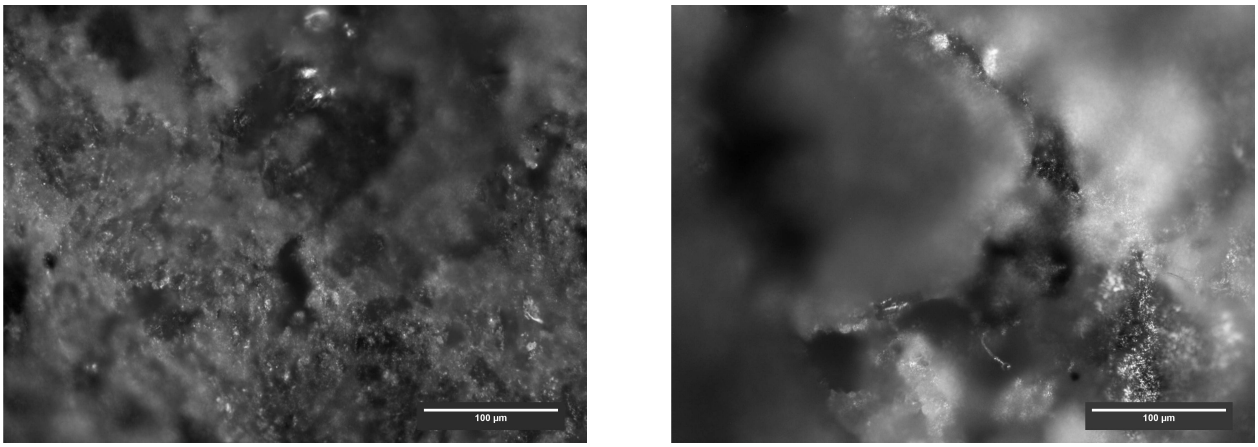

FIGURE 12. Micrographs of tight sand samples 4 and 5.

software tools used in image segmentation are public-domain codes ImageJ[4] and GraphicsMagick[5]. ImageMagick[6]is another command-line software tool, which implements algorithms used in this study, and can be used as well.

The procedure goes in several steps. Usually, the intensities histogram of the micro CT reconstructed image is concentrated in a part of the entire interval. This circumstance makes the selection of the threshold value more complicated since the contrast window must be zoomed into an interval close to the transition between solid and pore voxels. Thus, as the first step, the images of the 3D stack are normalized in a way that the histogram of intensities spreads

[4]See http://rsbweb.nih.gov/ij/, accessed on September 9, 2010.

[5]See http://www.graphicsmagick.org/, accessed on September 9, 2010.

[6]See http://www.imagemagick.org/script/index.php, accessed on September 9, 2010.

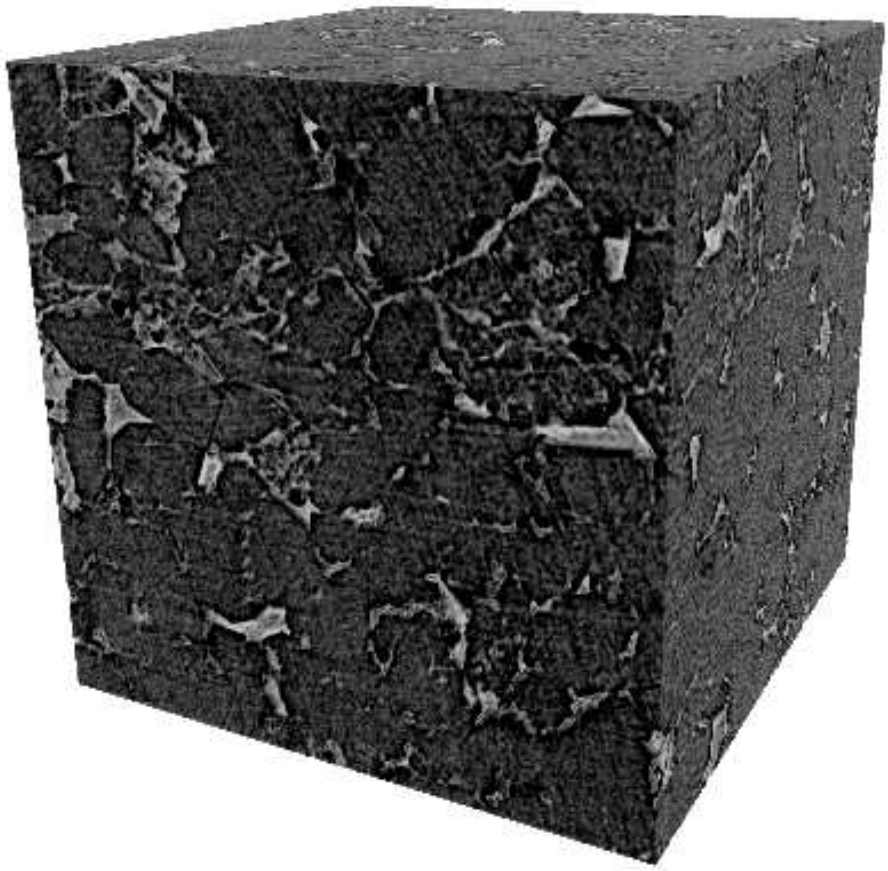

FIGURE 13. A 3D reconstruction of a tight sand sample. The cube edge is approximately 0.92 mm.

over a larger portion of the entire interval, which is between 0 and 255 in 8-bit image format. The reduced intensities interval is selected interactively, based on the histogram of the CT reconstruction. The input image format is tiff. To process a large image sequence, the GraphicsMagick commands are called from a SciLab[7] batch file. The image normalization procedure runs in a command-line mode. Note that the image sequence produced by CT reconstruction has no appreciable variation of the intensities between different layers. Therefore, the same image normalization parameters can be applied to all layers.

The next step is selection of the threshold value. Figure 15 shows a gray-scale layer of sample 1. The plot on the right-hand side shows the plot of intensities versus the distance along the line in the left-hand image. This line crosses a number of pores and grains. The plot shows that the

[7]See http://www.scilab.org/ script file, accessed on September 9, 2010.

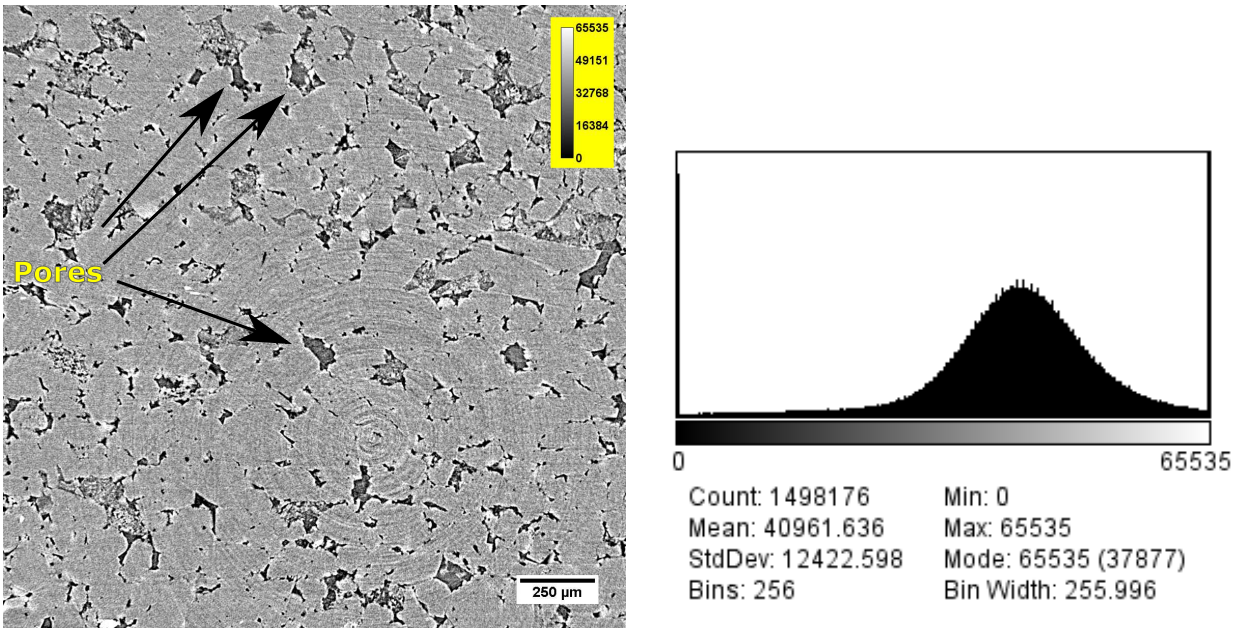

FIGURE 14. A reconstructed CT image of tight a sand sample at 1.7 micron resolution: due to small porosity, the histogram has only one peak.

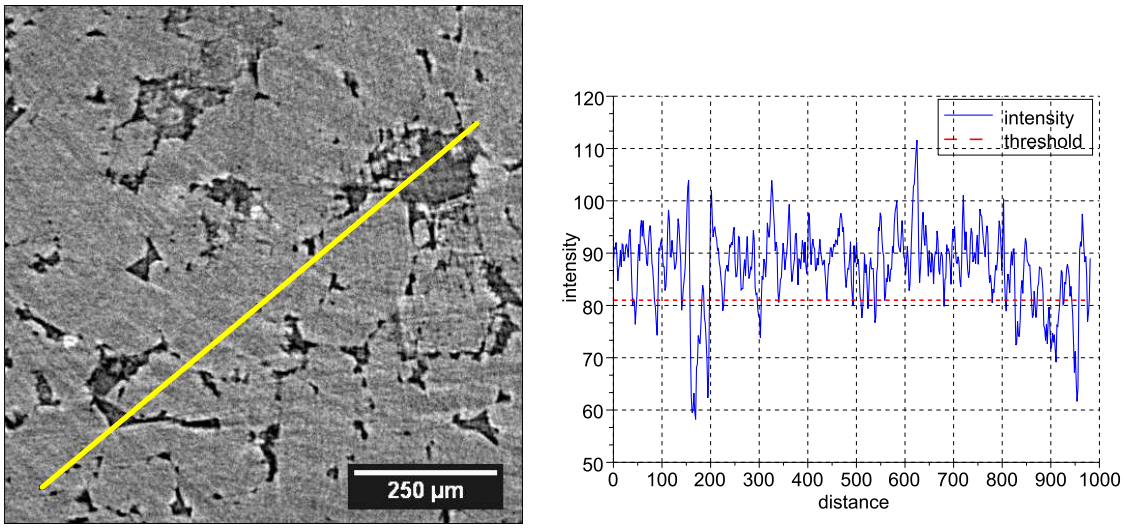

FIGURE 15. Choosing a threshold value using intensity map. The right-hand plot shows the intensity map along the line shown in the left-hand picture starting from the left bottom end.

respective intensities are separated. Inspection of the numerical values suggested the threshold value equal to 81.

Figure 16 shows the result of segmentation along with the original gray-scale image. The segmentation highlights some artifacts, which were not visible in in the original data. For

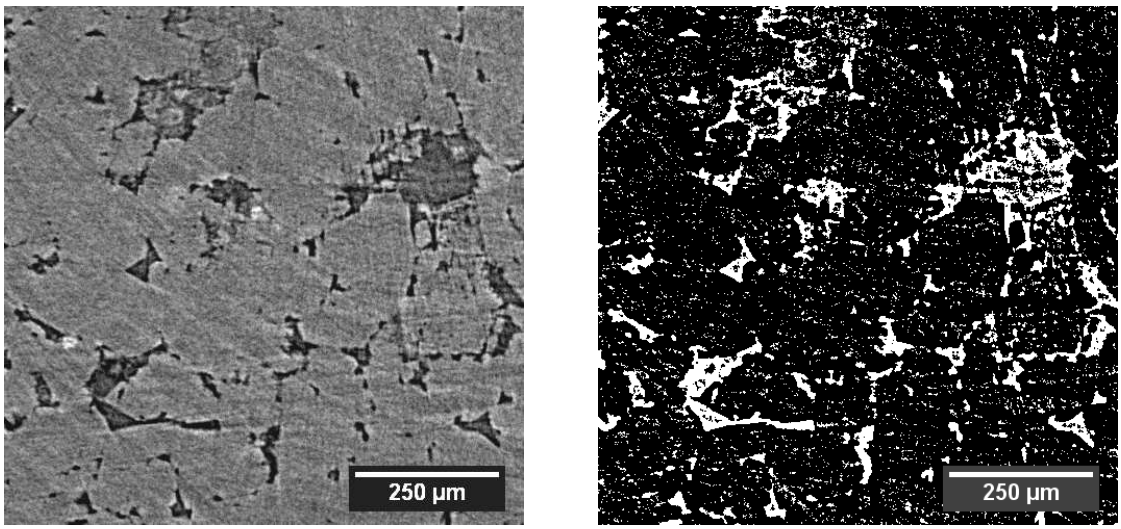

FIGURE 16. The original gray-scale image, left, and the result of segmentation with the threshold shown in Figure 15, right.

example, there is a noticeable amount of "salt and pepper" noise. The grains, shown in black, are covered with small white spots, and black dots randomly cover the pore space shown in white. Filtering out small clusters can significantly reduce the noise. The procedure used in this study is described in Section 3.3.

The thresholding and segmentation procedure described above involves a number of uncertainties. The selection of the threshold value is one of them. The decision on which parts of the image show pores, and which parts show the matrix is based on visual inspection and common sense. Validation of such an approach would require an independent high-resolution view inside the sample, which is practically impossible. The image of every slice includes margins, which are outside the sample. Seemingly, the intensity of marginal voxels, which are known to be in the void space, must define the threshold value. However, due to the noise in the data, such a procedure is unreliable. Figure 17 shows normalized histograms of voxel intensities evaluated in the matrix and in the void margins. The histograms are evaluated from the layer of sample 1 displayed in Figure 16. The threshold value of 81, which was selected above, turns out to be close to the abscissa of the intersection of the histograms. This value seems to be conservative with respect to overestimating the pore space. Figure 19 shows a plot of the porosity of the segmented image, evaluated by voxel counting for different threshold values. Porosity estimate for the chosen value 81 is 13.9 %. Figure 18 shows segmentations of the image from Figure 16 with the threshold values of 75 and 85. The pore space in the left-hand image reduces to slit-like

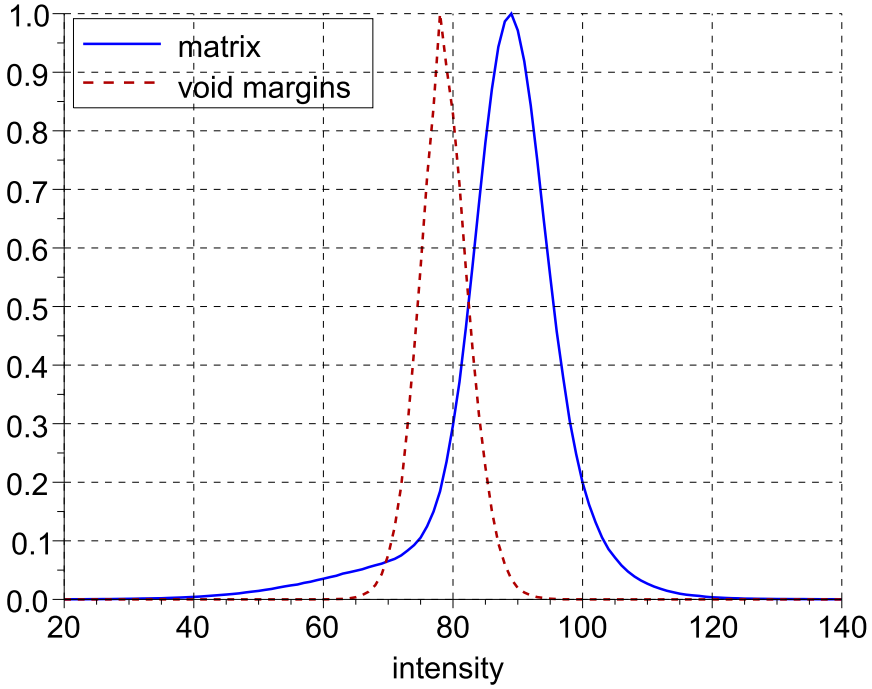

FIGURE 17. The histograms of intensities of marginal and matrix voxels overlap due to the noise in the digital data.

structures, while the right-hand image consists of a network of small white Variations of the threshold value do not eliminate the noise. Therefore, a noise-reduction procedure is needed. The next section describes such a procedure.

3.3. **Cluster-search cleanup of the digital data.** A segmented image may include a number of small clusters of solid-phase voxels inside pores, and clusters of pore voxels surrounded by solids. Such clusters may be physically linked to their phases by subresolution connections, but show up disconnected in the digital image just because the limited resolution of the x-ray tool or CT reconstruction errors. A disconnected cluster of solid-phase voxels inside the pore space is physically possible only if it is cut off by the image boundaries. On the contrary, isolated clusters of pore-voxels inside grains may physically exist. This fact makes image processing uncertain since no criterion can distinguish between physically and artificially isolated pores. However, even if isolated pores are physically present in the sample, they are "invisible" both for fluid flow and non-destructive porosimetry. The objective of simulations is to mimic the core laboratory measurements. Therefore, it makes sense to clean up the image from the isolated

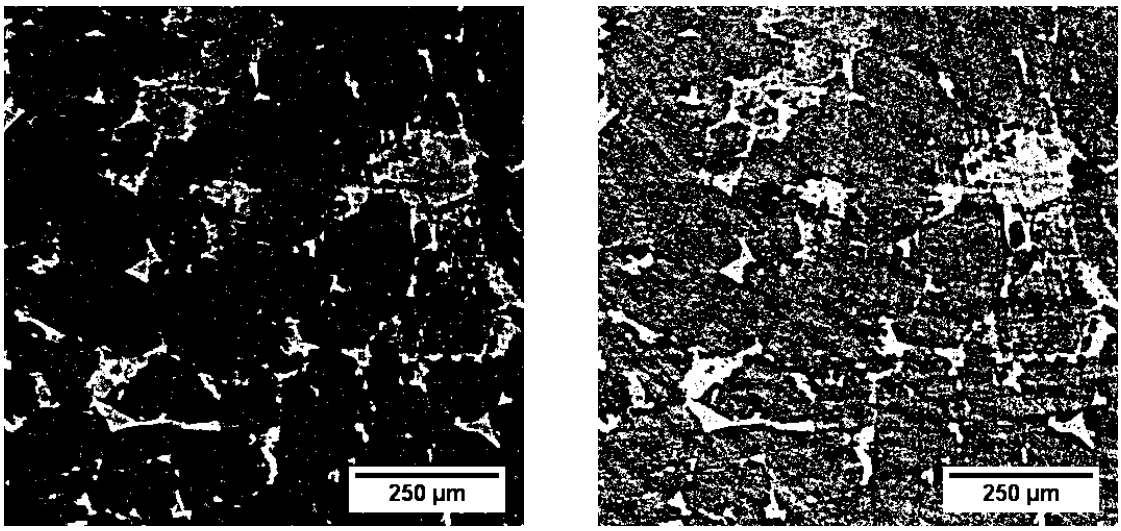

FIGURE 18. The result of segmentation of the gray-scale layer shown in Figure 16 with the threshold values of 75, left, and 85, right.

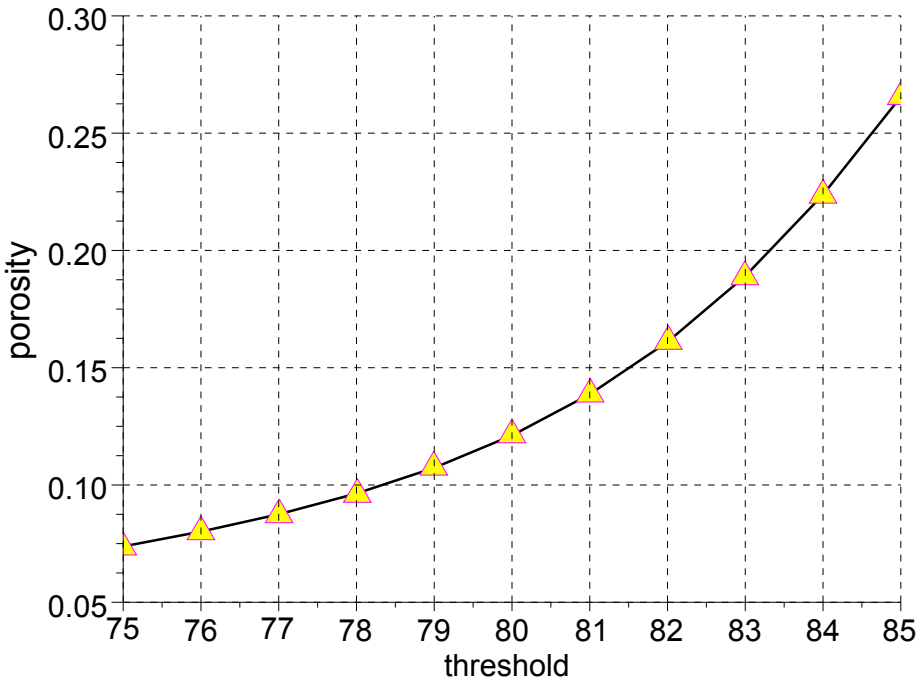

FIGURE 19. Porosity evaluated from segmented image versus the threshold value

clusters prior to the simulations. The isolated clusters can be removed, for example, by a cluster search algorithm [95].

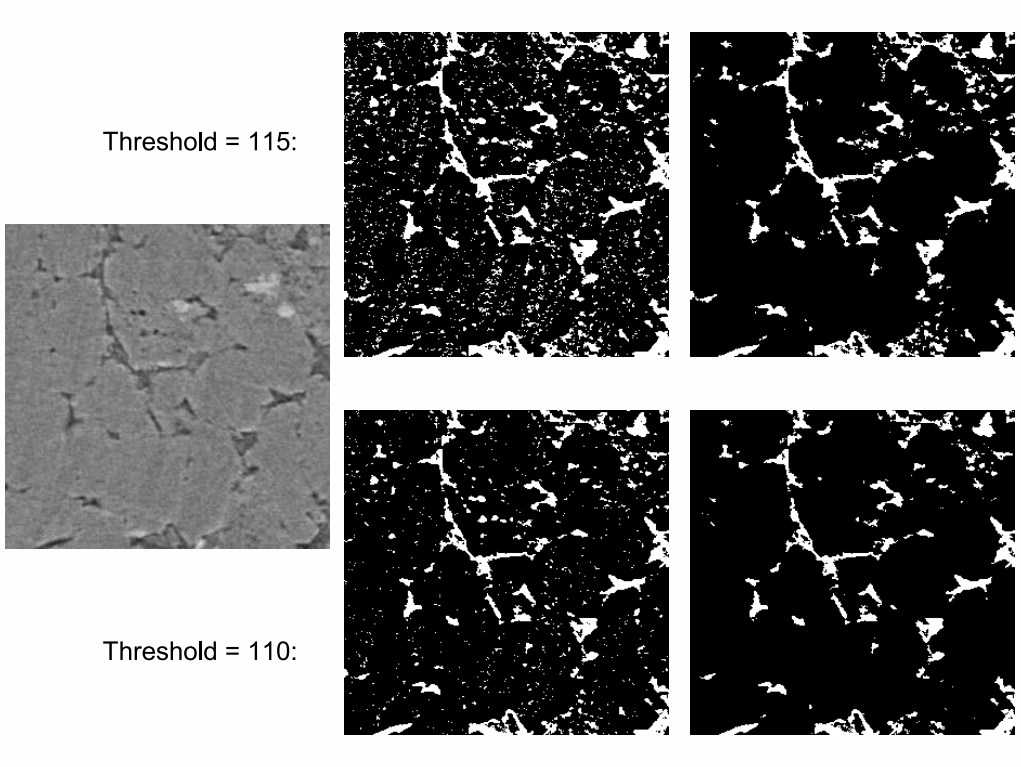

FIGURE 20. Segmentation and connectivity cleanup of the same gray-scale image for two threshold values.

The presence of isolated clusters and cluster sizes depend on the threshold value. Figure 20 shows two binary segmentation of the same gray-scale image (on the left). The rightmost column shows images after a cluster-search cleanup. Although a qualitative visual image inspection of a two-dimensional cross-section can be deceiving, it is obvious that the binary images are different, whereas their cleaned up versions have many similarities. Porosity evaluated from the binary image by pore voxels counting also depends on the threshold value, see Figure 19. However, it turns out that the capillary pressure evaluation is robust with respect to the segmentation threshold. An apparent reason is that threshold variations mostly affect the small gray-zone clusters, but do not dramatically affect the bulk part of the solid skeleton and the pore space. The last observation is in agreement with the successful evaluation of capillary-equilibrium fluid distribution from images strongly affected by noise reported in [97].

A two-dimensional cross-section may produce a misleading picture of connectivity. A large cluster intersected near its tip or narrowing by a plane will show up as a small spot. Therefore, cluster search must be performed on the entire 3D reconstruction.

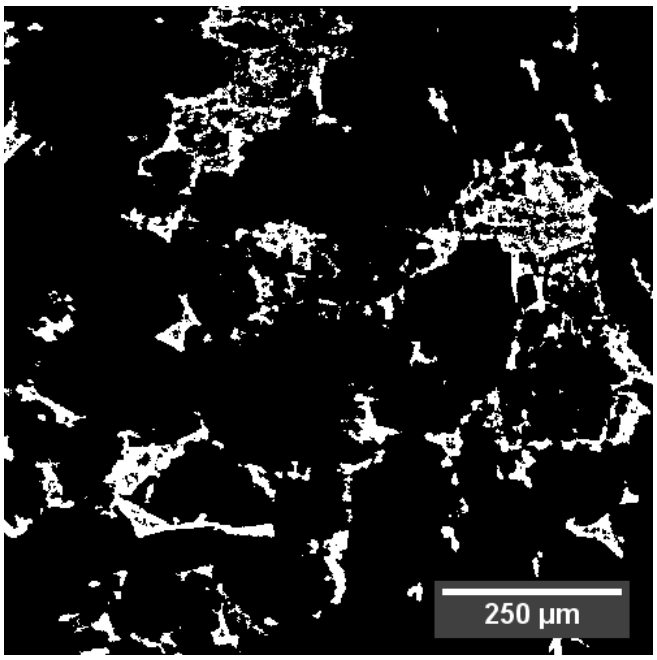

FIGURE 21. Result of data cleanup.

Figure 21 shows the result of removing clusters of 1000 or less voxels from the image of sample 1 shown in Figure 16. It was assumed that two pore voxels are connected if they have a common face, and two solid voxels are connected in they have at least one common vertex. After cleanup, the voxel-counting porosity estimate is 10 %, which is in an agreement with core test data. The image in Figure 21 still shows that the pores are filled with solid material. Apparently it is an indication of pore filling by clay particles, similar to those shown in the SEM image in Figure 7.

3.4. **MIS evaluation of the capillary pressure curves.** The idea of the method of Maximal Inscribed Sphere (MIS) has been described in [95, 97, 101]. The work [97] demonstrated that the predicted fluid distribution in the pores is in good agreement with the measurements, even when the input data is noisy. The computed capillary pressures reproduce mercury injection data. Previous work has been done for images of conventional sandstone samples and chalk. Here we focus on the application of the method to tight sands studies.

Based on the Young–Laplace equation, the MIS method evaluates the capillary pressure controlled fluid distribution in the pore space. The input data is a three-dimensional binary image of the pore space. For each pore voxel, the algorithm evaluates the maximal radius of a sphere

inside the pore space, which covers this voxel. Once this operation is done, different percolation schemes mimic drainage or imbibition fluid displacements. A displacement is modeled as a sequence of equilibrium configurations and does not account for the dynamic effects. Invasion percolation is suitable for modeling drainage, wheres simple percolation is more suitable for imbibition [62]. Gas is the nonwetting fluid. The wetting fluid could be either water or gas condensate. Material properties of the pore fluids and the solid and thermodynamic equilibrium determine the contact angle at an interface where both fluids and the solid are in contact [29, 30, 48, 53]. The very concept of contact angle assumes that the solid surface is ideally smooth and flat. Since in natural rocks the solid surface is usually rough and the grain shapes are irregular, a concept of effective contact angle is introduced [6]. The effective contact angle depends on the solid roughness and pore geometry and therefore is subject to uncertainty. In this study, we assume zero effective contact angle.

An inaccuracy in determination of the pore walls in segmentation will not affect the evaluation of the radius of an inscribed sphere as much as a single solid voxel incorrectly positioned in the middle of the pore. Therefore, the cleanup operation described above has a big impact on the capillary pressure evaluation. Figure 22 shows drainage capillary pressure curves computed from a segmented image before and after cluster-search cleanup. The points on the plots are computed from different images of the same sample. The size of the domains are 500 voxels cubed. The solid curve is an average value. Although at low capillary pressures the curves resemble each other very much, they become significantly different as the capillary pressure increases. The reason is that a large portion of the pore volume is disconnected in the raw binary image, and is never accessed by the invading nonwetting fluid. Figure 23 shows simulated gas distribution at two different saturations. On the left-hand picture, the gas saturation looks like a connected phase. On the right-hand side, it looks like caviar, since the phase is disconnected into bubbles separated by the wetting fluid. The bubble can form small clusters, when the pore size exceeds the capillary equilibrium interface radius. Mobilization of disconnected bubbles is blocked by the liquid fluid in the narrow channels connecting larger pores. Due to the extremely complex geometry, a visual inspection of a 3D picture cannot verify the connectivity of the fluid phase.

The closeness of the points to each other and to the mean curve indicates the representativeness of the image. In Figure 22, the invasion was simulated in all directions. Figure 3.4 shows capillary pressure curves computed by simulations of directional invasion in three coordinate

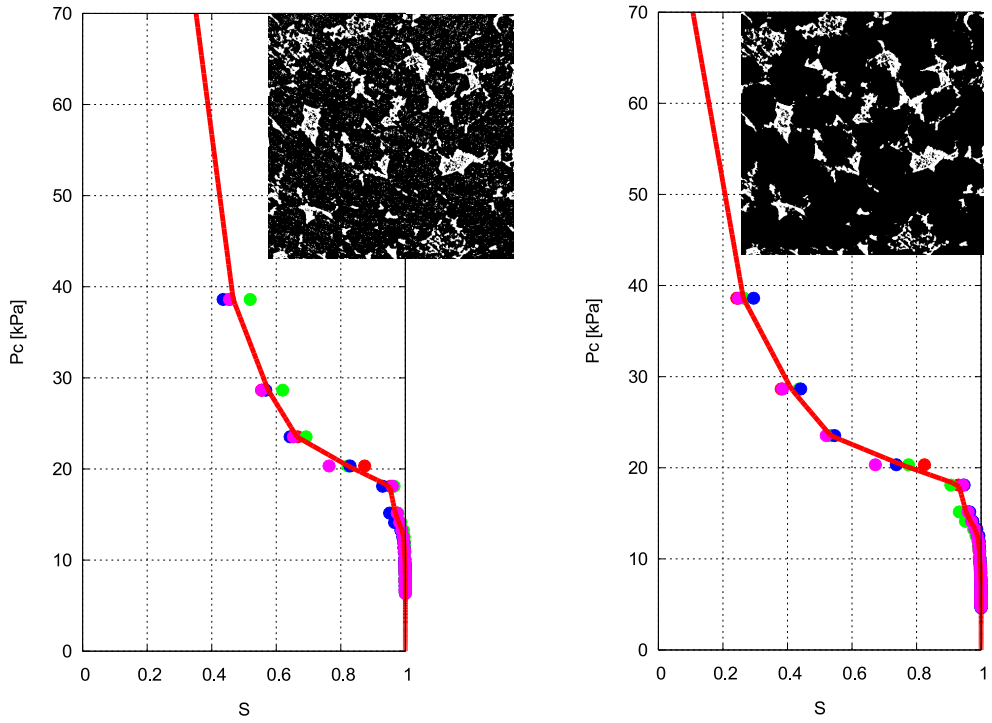

FIGURE 22. The impact of cluster-search cleanup on the capillary pressure curve evaluation.

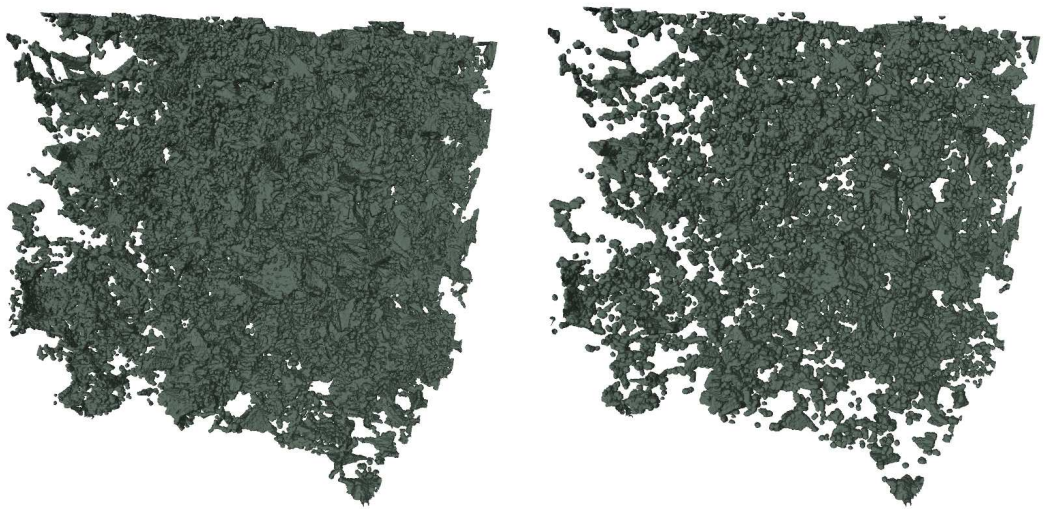

FIGURE 23. Computed gas distribution in the pores before (left) and after (right) being disconnected.

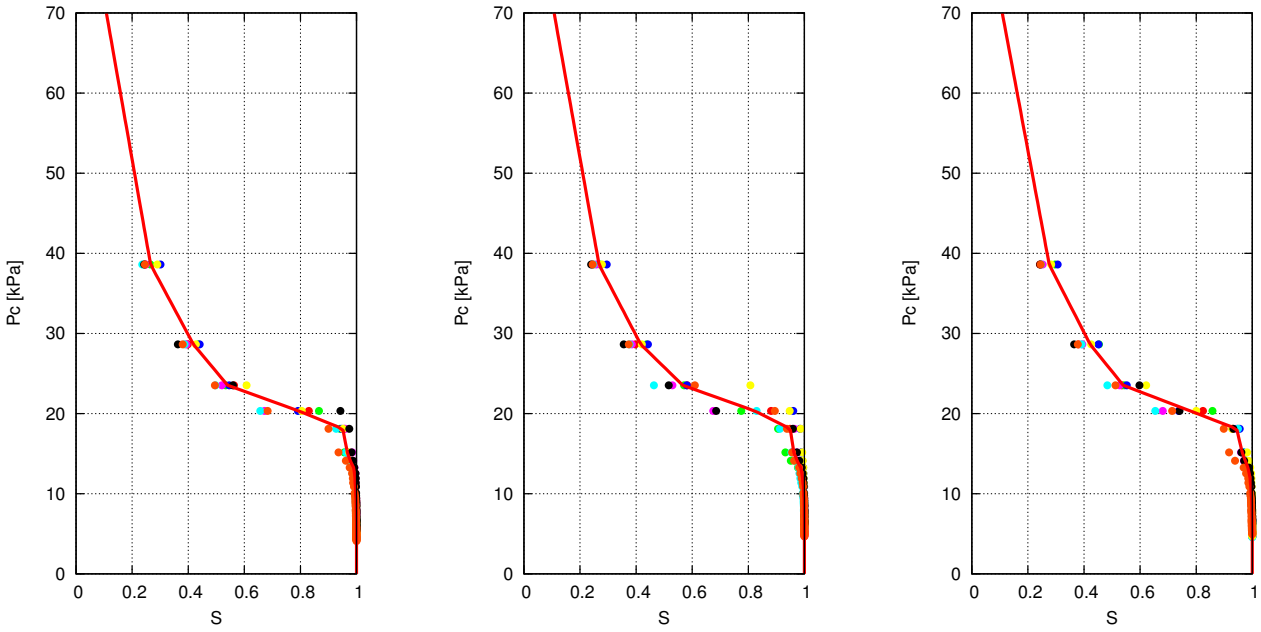

FIGURE 24. Capillary pressure curves evaluated from invasion percolation in three coordinate directions: x (left), y (middle), and z (right).

directions: x, y, and z. The computations were performed on a cluster-search clean image. The similarity of the results is another indication of representativeness of the volume.

Besides capillary pressure estimation, the method allows for evaluation of the connectivity of the phases. If the saturation of the wetting fluid is high, the nonwetting phase becomes disconnected into separate blobs and ganglia. Ordinary percolation simulations highlight a distinctive feature of tight sand samples: a relatively small volume of the wetting fluid can get the nonwetting phase disconnected. The estimates show a threshold saturation near 30 %. Apparently, in the studied tight sand samples, the cluster of relatively large pores are connected through very narrow channels. The wetting fluid can access these channels at a relatively low capillary pressure. The water encroaching due to the pore pressure depletion, can flow along the pore walls roughness. Retrograde gas condensation can create liquid saturation *in situ*. In either situation, the gas phase may become disconnected and the production will be blocked. The large aspect ratio between the dimensions of the pores and the connections between the pores not only blocks gas flow by a relatively small amount of water, but also may keep the water saturation low. Unusually low water saturation in tight gas sands was reported in [67], see also [79]. Water production is relatively rare in tight gas reservoirs, and water-blocking mechanism was used for explaining gas trapping [67].

Pressure maintenance could mitigate the blockage of gas flow. However, high pressure near the well will reduce the pressure gradient and slow down the flow. The optimal pressure is a compromise between water or condensate blockage prevention and keeping the gas flow into the well at economical value is not universal, but depends on the specific reservoir conditions and properties. A quantitative estimate of such an optimal compromise will be a subject of a separate study.

4. Simulation of the flow and evaluation of permeability

A segmented three-dimensional image of the pore space of a tight-sand sample provides natural discretization for flow simulations. We employ a Market-and-cell (MAC) scheme where the pressures are evaluated at the voxel centers, whereas the velocity components are evaluated at the voxel boundaries. Section A of Appendix describes the discretization in more detail. Even if the medium is isotropic with respect to permeability, a small sample can be non-isotropic due to the local heterogeneities. Therefore, the permeability tensor is evaluated by simulating the flow in three independent directions. To solve the system of equations generated by the finite-difference scheme, we need to add boundary conditions. For each coordinate direction, x, y, and z, the pressures at the inlet and outlet faces of the domain are equal to given values, and at the lateral boundaries pressures are linearly interpolated. At the pore walls inside the domain, no-slip or slip boundary condition can be applied depending on the objectives of simulations. At the inlet and outlet faces, the flow is directed parallel to the pressure gradient the normal derivative of the component parallel to the pressure gradient is equal to zero. For example, for simulating the flow in x direction, at the inlet face we approximate conditions $\dfrac{\partial v_x}{\partial x} = 0$, $v_y = 0$, and $v_z = 0$. At the lateral boundaries, we impose a "sleeve" condition modeling a core flow experiment with the lateral boundaries sealed by an impermeable sleeve. This selection differs from the boundary condition of the third kind employed in [96]. The reason is that in the cited paper the permeability was evaluated on an image of high-permeability conventional sand. Therefore, the lateral boundary effects were suppressed just by the fact that the domain was much larger in lateral dimensions that in the direction of the pressure gradient. It turned out that tight sands need a different approach. Just allowing the flow through the lateral boundary in conjunction with the Dirichlet boundary condition for pressures, created high-velocity flow. Due to the low permeability of the sample, this high flow still can significantly affect the permeability

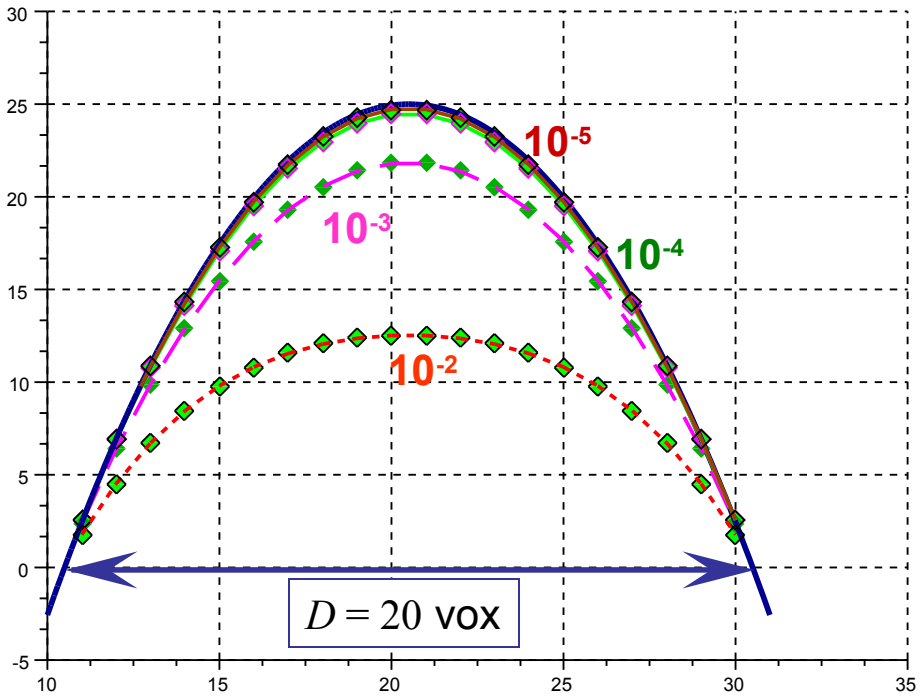

FIGURE 25. Poiseuille flow in a rectangular duct: numerical approximations, marked lines, versus the exact solution, solid line.

estimation, even though it is concentrated in a narrow layer near the boundary only. So, most simulations model an impermeable sleeve at the lateral boundaries of the domain.

It has been observed in [96] that the convergence criterion must be stringent. This requirement makes the problem computationally intensive. The procedure is only partially implicit, and it requires solving only one elliptic equation for pressures per one iteration step, versus four equations for pressures and each velocity component in a fully implicit scheme. Some not fully implicit schemes can be unstable. The stability is affected by the selection of the dimensionless "time step" τ and the viscosity coefficient η in the discretized Stokes equations. Perhaps thanks to the dimensionless form of the equations, once chosen τ and η became "universal": all simulations converged without developing instability.

Figure 25 shows flow velocity profiles in a 20-voxels wide rectangular duct. The solid line shows the exact Poiseuille solution, whereas the marked lines show numerical solutions obtained with different convergence criteria. Seemingly reasonable convergence for the relative error criterion of 10^{-5} may be insufficient for solving the Stokes problem of creeping flow around a sphere [96], or when the flow is in a complex-geometry pore space.

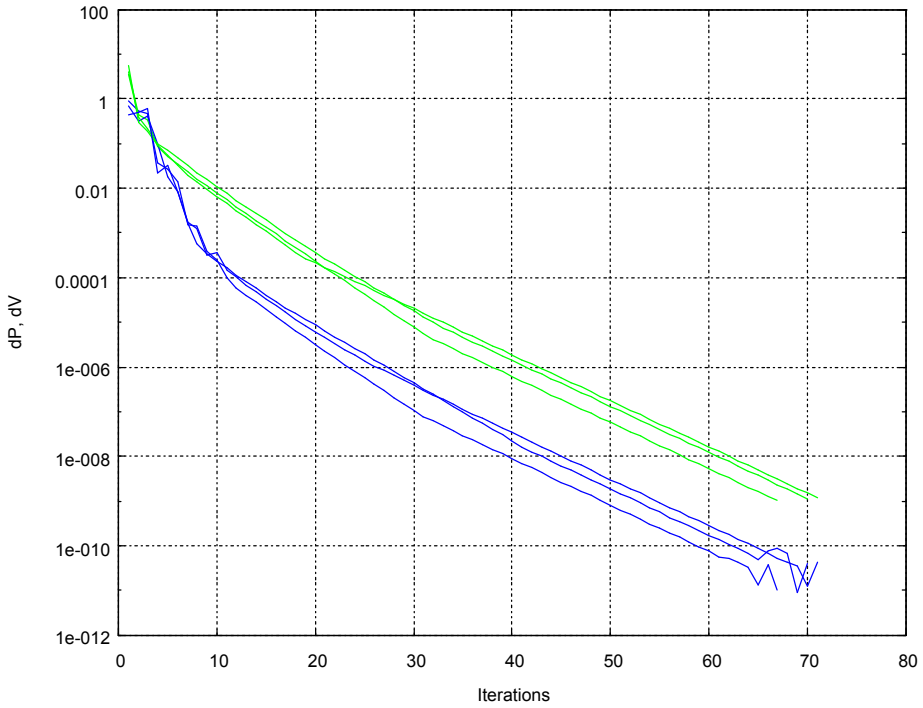

FIGURE 26. Linear convergence, on the left: the incremental value starts random fluctuations as the relative error goes below 10^{-11} indicating an apparent limit for the smallness of the convergence criterion.

Simulations of flow in a pore space demonstrate linear convergence, see Figure 26. However, iterations accelerate as they approach the solution. Therefore, the computer time needed to fulfill the criterion of relative increment of the order of 10^{-5} is not much less than the computer time needed for satisfy a orders of magnitude higher-accuracy criterion of 10^{-5}, Figure 27. This observation was confirmed in most simulations. We explain this acceleration in computations by the fact that as the iterations approaches the solution, the solution of the linear system of algebraic equations discretizing the boundary-value problem for pressures requires less and less time. Unfortunately, it is impossible to utilize this acceleration for fulfilling an even more stringent convergence criterion in a relatively short time. Figure 26 shows that random fluctuations coming from the round-off errors start impacting the iterations once the increment becomes very small, 10^{-10} in Figure 26.

With all the uncertainties of x-ray micro CT reconstruction, images of tight sand samples definitely show noticeable porosity variation even within a single sample image. Image subsampling and evaluation of permeability on image fragments make possible to evaluate the computed trend of porosity-permeability correlation. Kozeny–Carman correlation [19, 60] is a widely-used

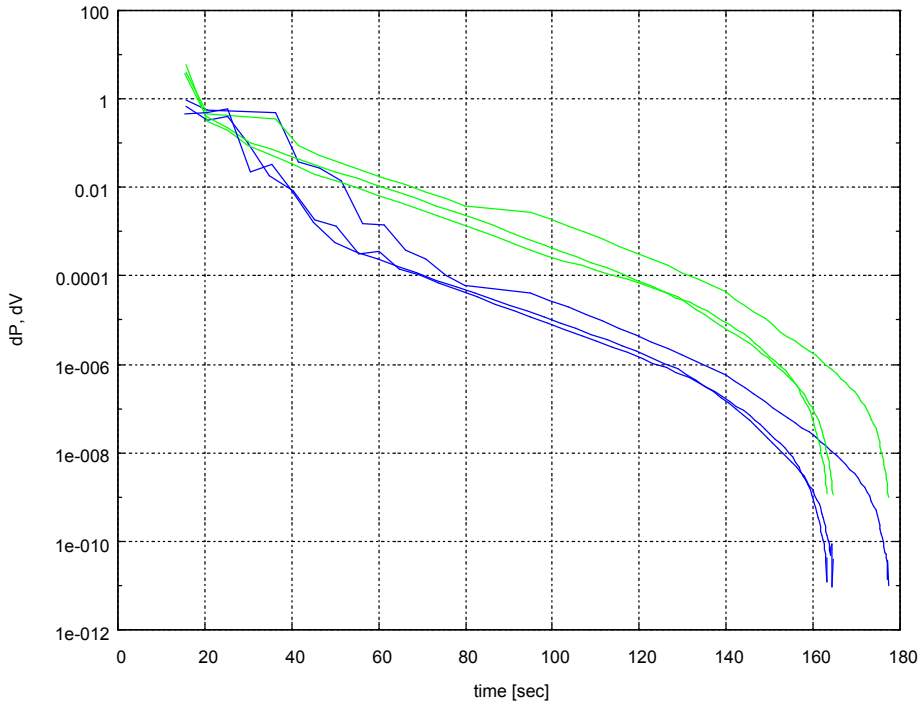

FIGURE 27. The computations accelerate after the increment achieves a threshold near 10^{-5}.

power-low expression of the permeability as a function of porosity. Numerous studies generalized and extended the Kozeny–Carman equation [45]. Recently, Krause *et al.* [61] pointed out that such a relationship may be in contradiction with the porosity–permeability correlation implied by the capillary pressure scaling law [68], which also is used for evaluating the permeability from porosity measurements [42, 100], including tight sands [27, 106]. Image subsampling and flow simulations shows a power-low trend. Figure 28 shows a log-log plot of simulation results for over 500 subsamples of a Fontainebleau sandstone sample with porosity range between 8 and 24 %. The high permeability estimates may be the result of the smallness of subsamples: they may not appropriately reflect the pore space tortuosity.

An picture on paper or on a screen only can show a two-dimensional projection of a three-dimensional structure. It is difficult to assess the complexity of 3D pore space geometry and to identify the connections between the pores just from visual inspection of the sample image. For example, the plot of streamlines in the left-hand picture of Figure 29 shows that some openings on the from face of the sample shown on the left-hand side are almost disconnected from the other pores. Figure 30 shows pressure distribution in the same sample. In general, pressure distribution is close to uniform gradient aligned with the flow direction. However, there are

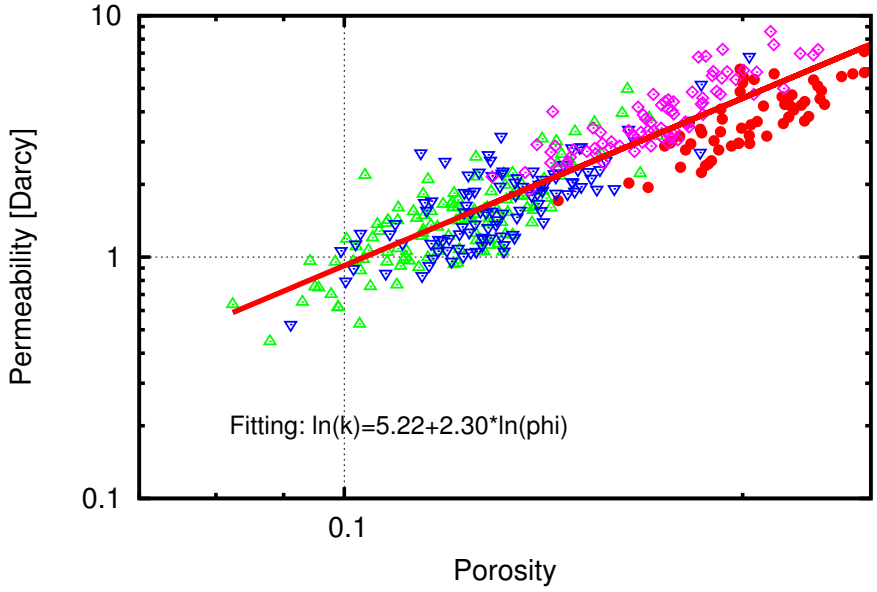

FIGURE 28. Power-low porosity-permeability correlation evaluated on 513 sub-samples of Fontainebleau sandstone

noticeable colored "tongues", which indicate small deviation of the pore pressure from linear distribution. Pressure gradient is not constant everywhere. For example, larger openings are covered by the same color indicating relatively low pressure gradient.

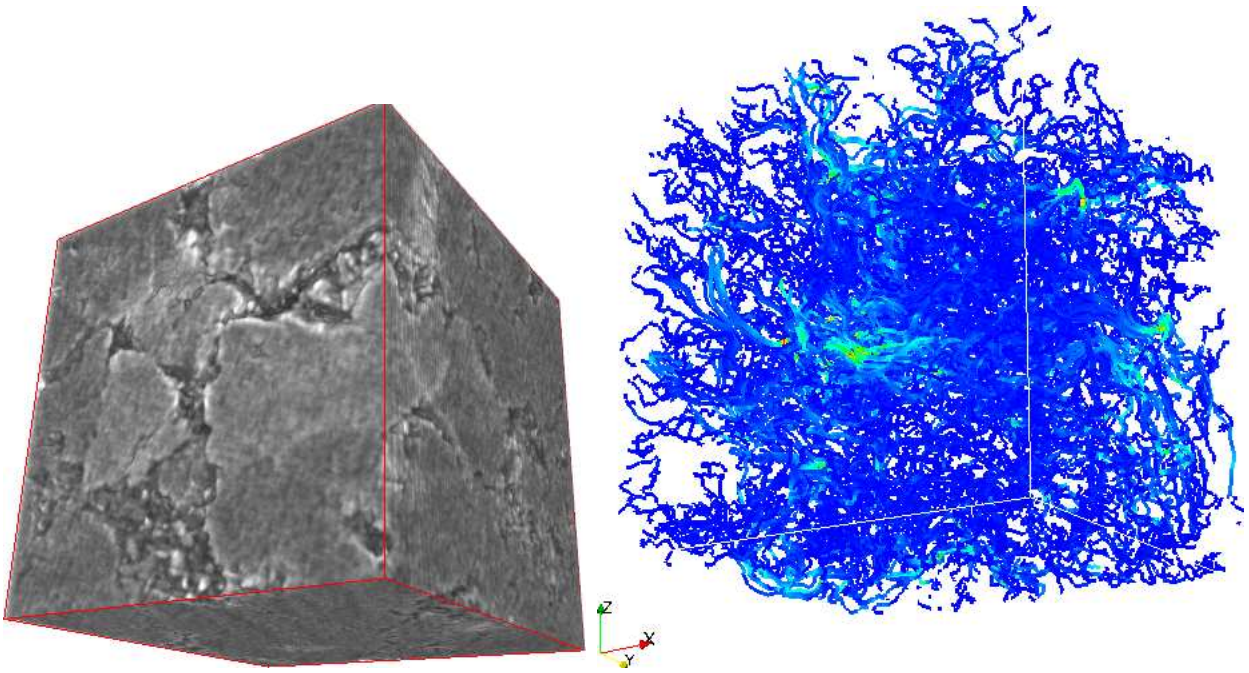

FIGURE 29. Plotting flow streamlines helps to understand the pore space structure and connectivity

4.1. **Estimating relative permeability curves.** In this study, evaluation of the relative permeability curves includes two steps. First, the capillarity dominated equilibrium fluid distribution is evaluated with the method of maximal inscribed spheres, see Section 3.4. Second, the permeability to each fluid phase is evaluated using the approach of Section 4. The dimensionless relative permeability curves are obtained by scaling the results with the computed absolute permeability. A similar approach was used in [96] for CT images of conventional sandstone samples. The method employs image partitioning into relatively narrow layers orthogonal to the pressure gradient. Since the pores are extremely small and the connecting channels are very narrow in tight sands, the method developed in [96] risks to overestimate the connectivity of each fluid phase. To avoid this overestimate, partitioning of the image into slices is not applied in this study. Instead, the connectivity of each phase is evaluated from the MIS-calculated output using cluster search algorithms. Note that MIS-calculations are significantly less computationally demanding than flow simulations. Therefore, the connectivity analysis can handle large data sets even on a reasonable-size personal workstation or a laptop. After connectivity analysis, the flow simulations for estimation of the permeability are conducted only on the voxels connected to the boundaries of the sample. Unlike in [96], the simulations employ a projection method

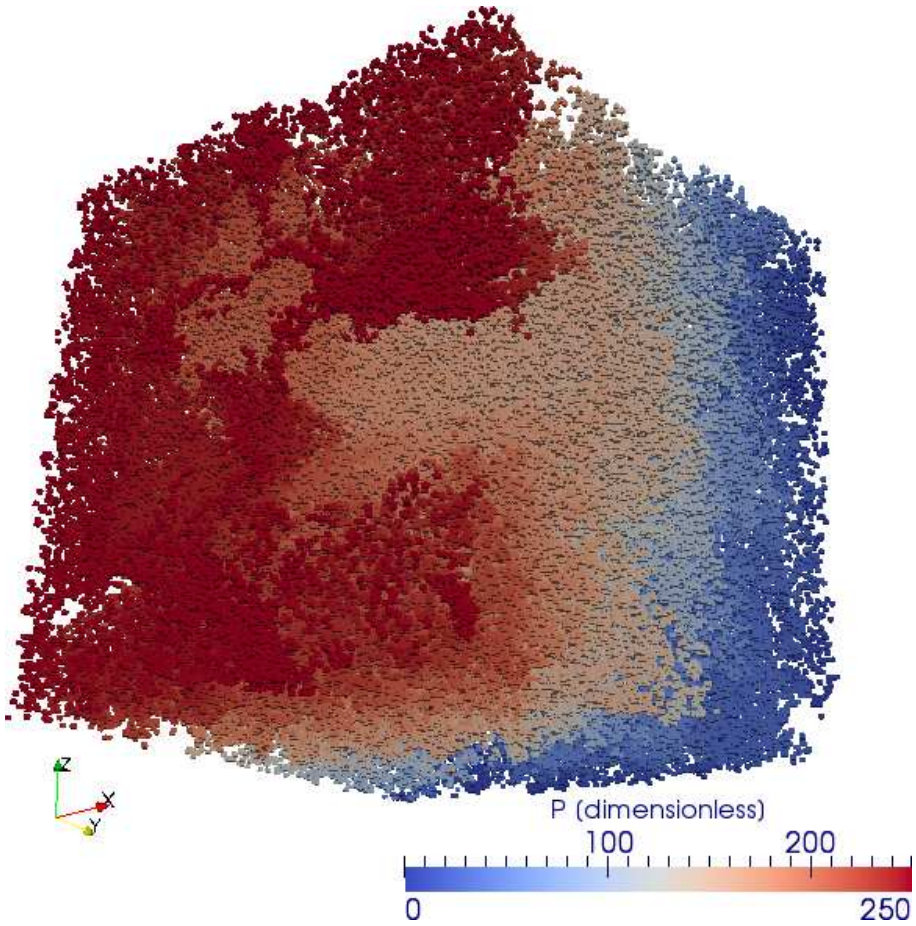

FIGURE 30. Dimensionless pressure distribution.

described in Section 4 and Appendix A. To make the code working on a desktop workstation, the computations are run on a number of subsamples and the individual results are averaged. As has been noted above, the computed absolute permeability is likely to overestimate the permeability measured on a core in the laboratory. The reasons could be in the coarseness of discretization, insufficient size to capture the tortuosity,

Due to extremely low permeability of tight sands, coreflood experiments are very difficult and time-consuming. Publications reporting relative permeability measurements are sparse [22, 89, 93, 104]. Since fluid mobility, which is the ratio of permeability and viscosity, eventually controls the flow, experimental evaluation of permeability to water is even more difficult. Not so many publications include water relative permeability curves [23]. Figure 31 shows plots of estimated relative permeability curves, which are shown as diamonds for imbibition and crosses for drainage. The average curves are shown as solid and dot-dashed line respectively. Laboratory

gas relative permeability data[8] displayed as triangles for imbibition and as squares for drainage. The number of data points on each curve is very limited. For the laboratory data, this is an implication of the low permeability and porosity. The computed points are not numerous by a similar reason: the pores are too small. Computations run in dimensionless numbers, so the smallness of pores in the last sentence refers to the size measured in voxels. Therefore, this size theoretically can be "increased" by refining the resolution of the image. However not always such a choice is feasible. Voxel size is constrained by the resolution of the imaging device and at the time of image acquisition it was 1.8 micron. Due to the small porosity, the pores occupy only a small part of the entire image. Therefore, a refinement of voxel size for better capturing pore geometry will result in a larger total image size. For example, reduction of voxel size by half increases the number of voxels by the factor of eight. Simulations on a very large image may require computer super power.

Figure 32 shows the results of drainage and imbibition relative permeability evaluation on a micro-CT of a sample different from the one in Figure 31. In drainage simulations, the nonwetting fluid can occupy only the voxels connected to the boundaries. A number of common features are confirmed in all simulations. The nonwetting fluid relative permeability data points are more scattered than those for the wetting fluid. This observation holds valid for conventional rocks too [96]. Apparently, the reason for scattering is the same: the possibility of the nonwetting phase to get disconnected. This explanation is supported by the observation that in drainage, the scattering in the nonwetting permeability data is less, see Figure 32. The relative permeability to gas vanishes as brine saturation approaches 30–40 %. The curve is concave, so that the decay of permeability to gas accelerates as the water saturation increases. Qualitatively, this observation is not surprising since Section 3.4 has already remarked that a relatively low water water saturation makes the gas phase disconnected, Figure 23. Theoretically, the disconnected phase can flow. But it seems to be impossible for the studied samples since it would require a pressure gradient sufficient to break water bridges in the narrow pores. It is unfeasible in field conditions. The absolute permeability of the rock is small, and water viscosity exceeds that of gas by orders of magnitude. Therefore, in the range of saturations, where the gas relative permeability is zero and water relative permeability is close to zero, the gas is immobile and the water mobility is low. This observation explains the pore-scale nature of "Permeability

[8]The data and the sample are courtesy of Chevron.

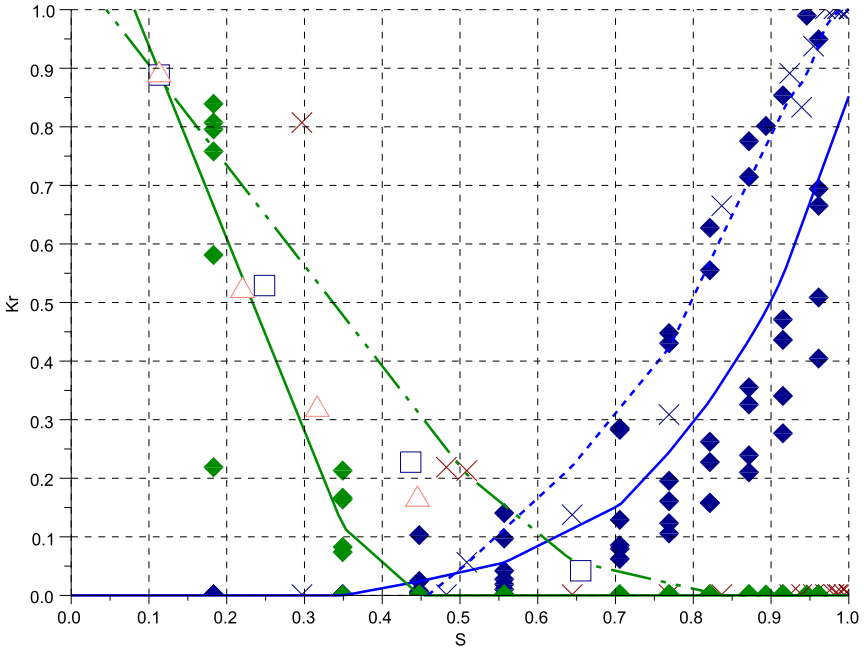

FIGURE 31. Computed relative permeability data (diamonds for imbibition and crosses for drainage) and laboratory measurements (triangles for imbibition and squares for drainage) of gas relative permeability for different water saturations. The solid lines display mean computed imbibition relative permeability curves, and the dashed curves show mean computed drainage relative permeability curves. The laboratory data are courtesy of Chevron.

Jail" [23, 93], which is a range of saturations where both fluids, gas and water, are immobile. Note that the nature of gas trapping is capillarity: the geometry of the pore space creates a distributed capillary barrier to gas flow by breaking gas connectivity by water. The nature of water trapping is dynamic: although water as the wetting phase and is connected through the corners and crevices in the pores, the low permeability of the rock and relatively high water viscosity makes it practically immobile. Thus, one may say that in the Permeability Jail, the gas is the prisoner guarded by the water or condensate, even though the latter is derived from gas.

Note that the drainage relative permeability curves in Figures 31 and 32 do not show Permeability Jail. In drainage, the invading nonwetting fluid remains connected. The gas distribution

does not include a dispersed component, so the permeability to gas is higher than at the same brine saturation in imbibition (or condensate dropout, see below). Similarly, the dispersed gas bubbles or ganglia, which likely to develop in imbibition, do not develop in drainage, so the permeability to brine is higher as well.

In a sense, the two types of computed relative permeability curves correspond to two extreme situations. The computed drainage relative permeability is evaluated based on the assumption that the gas phase is always connected to the boundaries of the sample. In this approach, the dispersed component [47] of gas saturation is assumed to be equal to zero. The imbibition curves assume that the nonwetting phase occupies all space that is accessible to gas at the given capillary pressure. Some gas clusters may be disconnected from each other and from the boundaries. In this approach, the dispersed component of gas saturation is at admissible maximum at a given capillary pressure. The latter situation more adequately describes equilibrium fluid distribution resulting from gas condensate dropout, where the latter is controlled by the thermodynamic conditions and may occur anywhere in the pore space regardless of the connectedness to the boundary. It is reasonable to assume that in a laboratory experiment or in the reservoir the fluid distribution is somewhere in-between the described extreme configurations. The relative position of the computed relative permeability curves and laboratory data points on the plots in Figure 31 is an illustration to this remark.

Relative permeability curve evaluated from network simulation has been reported in [76]. In this work, the grains are modeled as spheres. At low saturations, the wetting phase forms rings and bridges. It is concluded that these structures are the primary mechanisms for water sensitivity in tight gas sands. An earlier work [28] reported on experimental investigation of the impact of wettability on the dropout of condensate. It is remarked that in presence of water, the pendular rings and bridges between hydrophilic spherical grains are enhanced by the condensate, since the latter creates films between the water and gas. Experimental studies on enhancement of condensate flow by alteration of wettability were reported in [81].

5. Application: a model of gas trapping by retrograde condensation.

Gas production in tights sand reservoir is a complex process. The extremely low matrix permeability does not allow for economically viable production unless the wells are stimulated by hydrofracturing [49, 78]. A connected network of natural and created fractures connects the

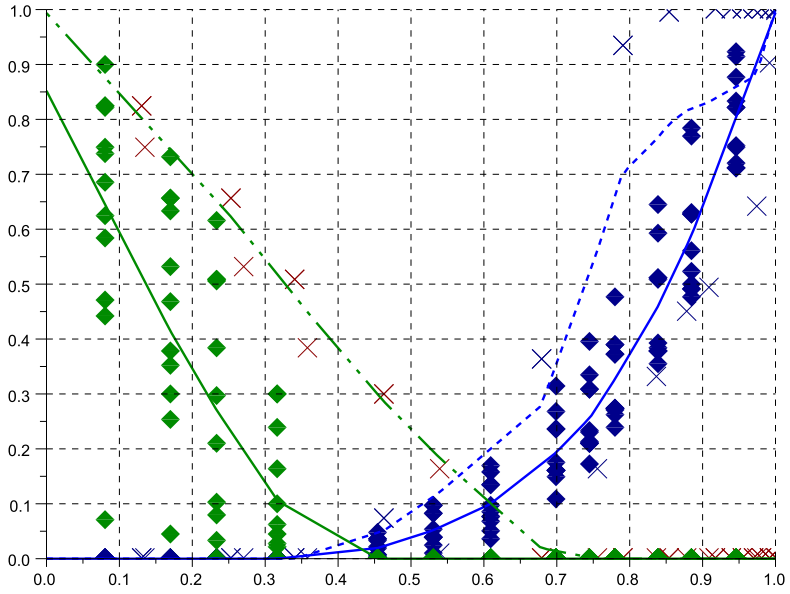

FIGURE 32. Evaluation of relative permeability curves using MIS analysis and flow simulations. Diamonds denote imbibition relative permeabilities, the crosses correspond to drainage. The solid lines show mean imbibition, and the dashed lines show mean drainage curves.

well to the reservoir. The gas is stored in the matrix blocks. Thus, to be produced, the gas first has to flow from the matrix blocks into the adjacent fractures. Compaction caused by pressure depletion, pores clogging by particles transported with gas, condensate dropout, all are capable to adversely affect the permeability to gas and hinder production. Here we focus on the impact of retrograde condensation. We narrowly focus on the phenomena occurring at the interface between the matrix and the adjacent fractures.

Natural gas composition consists mostly of methane molecules, but it also may contain many other hydrocarbons and non hydrocarbon compounds. Depending on the pressure and temperature conditions, these other compounds may be present in gas or liquid phases, or both. Natural gas is called wet or dry depending on how large is the liquefiable portion of gas composition.

Equilibrium distribution of each components between the gas and liquid phases is determined by the equality between chemical potentials. Figure 33 shows a cartoon of thermodynamic-equilibrium phase diagram of a reservoir hydrocarbon mixture. Consider a scenario where the

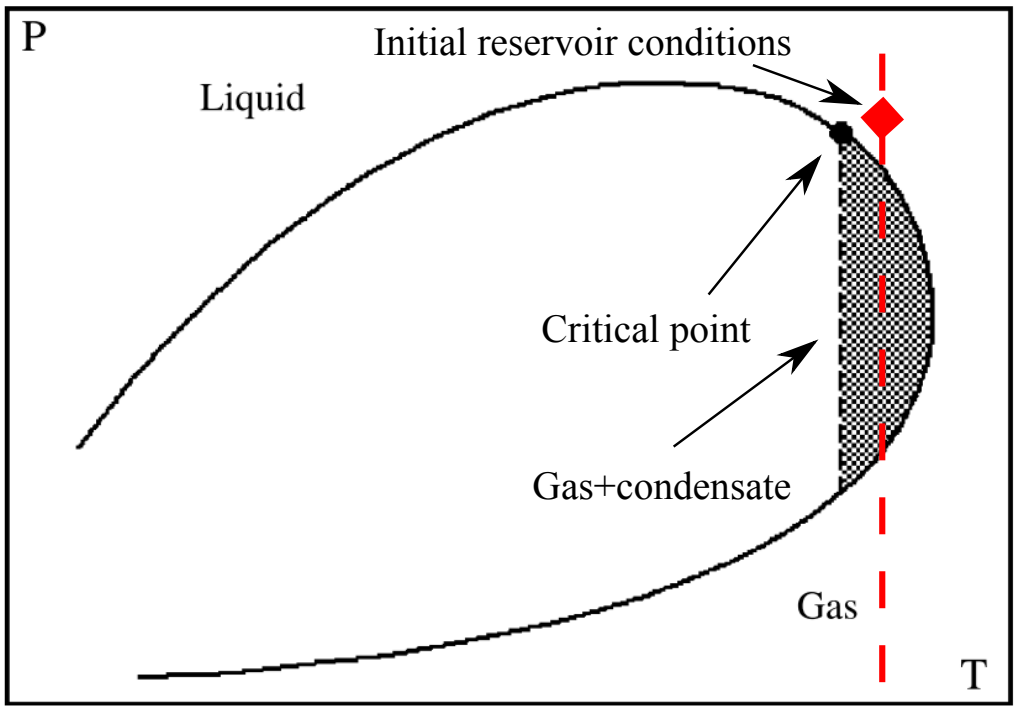

FIGURE 33. Phase diagram of hydrocarbon mixture, a modification of [85, Figure 1]. The shaded zone denotes gas-condensate system, the dashed line corresponds to the reservoir temperature, and the diamond denotes the initial reservoir conditions.

diamond denotes the initial reservoir pressure and temperature conditions. Pressure depletion will move the point on the pressure–temperature point downwards, toward the shaded zone in which some hydrocarbon components will dropout from the gas mixture into liquid. This phenomenon is called retrograde condensation. The term reflects the fact that pressure depletion results in condensation, as opposed to evaporation.

The lowest *in situ* pressure is near the wellbore. Simulations demonstrate that in a homogeneous reservoir the condensate saturation will be the highest near the wellbore [1, 20, 36, 73]. In case of near-wellbore damage with negative skin effect, condensate accumulates at the downstream interface between the low-permeability and high-permeability domains [84, 85]. In all cases, condensate dropout reduces the pore space available for gas flow. It reduces the effective permeability to gas and is considered reservoir damage [12, 37]. In a fractured conventional reservoir, the accumulating condensate can become mobile after reaching a certain saturation

threshold and produced by gravity-drainage [20, 36]. In tight sand, if small amount of condensate drops out near matrix-fracture interface, the Permeability Jail and the dynamic condensate blocking discussed in Section 4.1 make condensate production mechanisms inefficient.

We simplify the model by Panfilov and co-workers [84, 85], in order to emphasize the main aspects of interaction between flow and thermodynamics in gas condensation. We assume that no significant cooling or heating takes place, so that the density of the wet gas mixture, ϱ_g, is a function of pressure only: $\varrho_g = \varrho_g(p)$. Wet gas is the sum of dry component, which remains in gas phase within the range of interest, and the liquefiable component, which is in gas phase but may drop out in liquid if the pressure drops sufficiently, see [5]. Let c denote the mass fraction of the liquifiable gas phase in wet gas in thermodynamic equilibrium. Concentration c is a lumped quantity. A real gas mixture is multicomponent and each component concentration depends on all other concentrations. Therefore, the lumped concentration, c, depends on the initial wet gas mixture composition, the history of pressure depletion, *etc.* However, not all components equally contribute to the equilibrium and condensation at given conditions. Rather one component usually controls the lumped concentration variation at pressure depletion [85]. Therefore using just a single condensate concentration parameter $c(p)$ is satisfactory for the purposes of present studies. In isothermal conditions, c is a function of pressure only: $c = c(p)$. Not all liquifiable components will necessarily dropout from the gas phase within the range of pressures under consideration. Some liquifiable components may be produced and will have to be removed by gas treatment facilities on the surface. Therefore, the absolute value of $c(p)$ is subject to convention: it may or may not include these liquifiable components. However, as long as the thermodynamic equilibrium assumption holds true, the variations of $c(p)$ are determined uniquely by the pressure variations while gas is making its way to the well and to the surface.

The gas and liquid condensate are not mixing. Let $\mathbf{w}_g$ and $\mathbf{w}_l$ be the Darcy velocities of the gas and liquid phase respectively, and denote by S the condensate saturation, that is the relative volume of the pores occupied by the liquid phase. Mass balance equations for the dry and liquifiable components of wet gas are:

$$\frac{\partial}{\partial t}\left[\phi(1-S)(1-c(p))\varrho_g(p)\right] + \nabla\cdot\left[\varrho_g(p)(1-c(p))\mathbf{w}_g\right] = 0 \tag{1}$$

$$\frac{\partial}{\partial t}\left[\phi(1-S)c(p)\varrho_g(p) + \varrho_l S\phi\right] + \nabla\cdot\left(\varrho_g(p)c(p)\mathbf{w}_g\right) + \nabla\cdot\left(\varrho_l\mathbf{w}_l\right) = 0 \tag{2}$$

Here ϱ_l is the density of the liquid phase. Since the condensate composition is pressure-dependent, the liquid density ϱ_l also is a function of pressure. Assume that the matrix is isotropic and homogeneous, and its permeability and porosity are denoted by k and ϕ, respectively. From the Darcy's law,

$$\mathbf{w}_g = -\frac{kk_g}{\mu_g}(\nabla p - \varrho_g \mathbf{g}) \tag{3}$$

$$\mathbf{w}_l = -\frac{kk_l}{\mu_l}(\nabla p_l - \varrho_l \mathbf{g}) \tag{4}$$

Here $k_i = k_i(s)$ are the relative permeabilities of gas and liquid, and $\mu_i = \mu_i(p_i)$ are the viscosities, $i = g, l$, $\mathbf{g}$ is the gravity acceleration. The relative permeabilities depend on the condensate saturation, whereas the viscosities are functions of phase pressures.

We will focus on the saturations not exceeding the permeability barrier saturation. With this assumption, the relative permeability to condensate vanishes, and so does the last term on the left-hand side of Equation (2). We further assume steady flow, so that the time derivatives of the pressures are equal to zero. Consequently, the time derivatives of the densities, viscosities, and the condensate mass concentration in the wet gas mixture, vanish as well. In a layered formation, the permeability across the bedding plane is much smaller than that along the layers. If the dipping angle is mild, the gravity term in Equation (3) can be neglected. Thus, Equations (1)–(2) take on a simpler form:

$$-\phi(1-c(p))\varrho_g(p)\frac{\partial S}{\partial t} + \frac{d}{dp}\left[\varrho_g(p)(1-c(p))\right]\nabla p \cdot \mathbf{w}_g + \varrho_g(p)(1-c(p))\nabla \cdot \mathbf{w}_g = 0 \tag{5}$$

$$\left[-\phi c(p)\varrho_g(p) + \varrho_l \phi\right]\frac{\partial S}{\partial t} + \frac{d}{dp}\left[\varrho_g(p)c(p)\right]\nabla p \cdot \mathbf{w}_g + \varrho_g(p)c(p)\nabla \cdot \mathbf{w}_g = 0 \tag{6}$$

Multiplication of Equation (5) by $\dfrac{c(p)}{1-c(p)}$ yields

$$-\phi c(p)\varrho_g(p)\frac{\partial S}{\partial t} + \frac{c(p)}{1-c(p)}\frac{d}{dp}\left[\varrho_g(p)(1-c(p))\right]\nabla p \cdot \mathbf{w}_g + \varrho_g(p)c(p)\nabla \cdot \mathbf{w}_g = 0 \tag{7}$$

A subtraction of the last equation from Equation (6) eliminates the divergence of Darcy velocity. Thus, after substitution of the Darcy's law,

$$\varrho_l \phi \frac{\partial S}{\partial t} = A(p)\frac{kk_{rg}(S)}{\mu_g(p)}\nabla p \cdot \nabla p \tag{8}$$

where

$$A(p) = \frac{1}{1-c(p)}\frac{d}{dp}\left[\varrho_g(p)c(p)\right] - \frac{c(p)}{1-c(p)}\varrho_g'(p) = \frac{\varrho_g(p)c'(p)}{1-c(p)} \tag{9}$$

The coefficient $A(p)$ is a function of the wet gas composition in thermodynamic equilibrium. In retrograde condensation, the liquifiable gas phase concentration increases with pressure, so $A(p) > 0$. The conclusion that the rate of condensation is proportional to the pressure gradient squared, Equation (8) has practical implications. The pressure drops at the matrix-fracture interface more than inside the matrix. At early times, a pulse pressure decrease near the wellbore can create a narrow zone of intensive condensate dropout, which may block the gas flow when the saturation will reach the permeability jail zone. A smooth start with gradual pressure depletion will not prevent the condensate dropout entirely, but will slow it down and distribute the affected zone over a larger volume. Therefore, the chances that gas will continue flow unblocked by condensate over a prolonged period of time will increase. An optimal recovery rate and its dependence on the reservoir properties is a subject of a separate study.

Let us inspect how the model described above can be translated in pore-scale. We employ the same assumptions as above: the concentration of liquifiable components in the gas is determined by thermodynamic equilibrium, and, therefore, is a function of pressure. The flow is creeping and steady-state, so it is governed by the Stokes equations [66]. Let $\mathbf{u}_g$ denote the local gas flow velocity. Then, mass conservation for the gas phase reads:

$$\frac{\partial}{\partial t}\left[(1-c(p))\varrho_g(p))\right] + \nabla\cdot\left[(1-c(p))\varrho_g(p))\mathbf{u}_g\right] = 0 \tag{10}$$

The condensate dropped out from the wet gas mixture behaves as wetting fluid, so it sticks to the pore walls. If irreducible-water film covers the grains, then the condensate will attach to water as an oily film [12]. Whether water is present or not, the gas phase will remain in the central parts of the pores. Thus, in the total gas flow, the condensate dropout can be modeled as a sink term reflecting that some liquifiable components of the gas mixture condensed:

$$\frac{\partial\varrho_g(p)}{\partial t} + \nabla\cdot\left[\varrho_g(p)\mathbf{u}_g\right] = Q_{lc} \tag{11}$$

In steady state, time derivatives vanish, so Equations (10)–(11) yield

$$Q_{lc} = \nabla\cdot\left(c(p)\varrho_g(p)\mathbf{u}_g\right) = \frac{d}{dp}\left(c(p)\varrho_g(p)\right)\nabla p\cdot\mathbf{u}_g \tag{12}$$

Note that the pressure gradient is not necessarily parallel to the local flow velocity vector. For example, for Stokes flow with velocity $\mathbf{u}$ near a sphere of radius R centered at the origin,

the local velocity and pressure are is given by

$$\mathbf{v} = -\frac{3R}{4}\frac{\mathbf{u}+(\mathbf{u}\cdot\mathbf{n})\mathbf{n}}{r} + \frac{R^3}{4}\frac{3(\mathbf{u}\cdot\mathbf{n})\mathbf{n}-\mathbf{u}}{r^3} + \mathbf{u} \tag{13}$$

$$p = p_0 - \frac{3}{2}\mu\frac{\mathbf{u}\cdot\mathbf{n}}{r^2}R \tag{14}$$

see [66]. Here r is the distance to the center of the sphere, p_0 is the pressure far from the sphere, and $\mathbf{n}$ is the unit vector co-directed with the radius-vector $\mathbf{r}$, so that $\mathbf{n} = \frac{\mathbf{r}}{|\mathbf{r}|}$. A rearrangement of Equation (15) and differentiation of Equation (14) yield

$$\mathbf{v} = -\frac{R}{4r}\left(1-\frac{R^2}{r^2}\right)[3(\mathbf{u}\cdot\mathbf{n})\mathbf{n}-\mathbf{u}] + \left(1-\frac{R}{r}\right)\mathbf{u} \tag{15}$$

$$\nabla p = \frac{3}{2}\frac{\mu R}{r^3}[3(\mathbf{u}\cdot\mathbf{n})\mathbf{n}-\mathbf{u}] \tag{16}$$

Finally,

$$\mathbf{v} = -\frac{r^2-R^2}{6\mu}\nabla p + \left(1-\frac{R}{r}\right)\mathbf{u} \tag{17}$$

and

$$\nabla p\cdot\mathbf{v} = -\frac{r^2-R^2}{6\mu}\nabla p\cdot\nabla p + \left(1-\frac{R}{r}\right)\frac{3}{2}\frac{\mu R}{r^3}\left[3(\mathbf{u}\cdot\mathbf{n})^2-\mathbf{u}\cdot\mathbf{u}\right] \tag{18}$$

By virtue of Equation (16), the vector defined by the last term in Equation (18) is parallel to ∇p only if $\mathbf{n}$ is parallel to $\mathbf{u}$. Thus, the dot product on the loft-hand side in Equation (18) cannot be expressed exclusively through $\nabla p\cdot\nabla p$.

Consider another example: flow in a capillary tube of variable diameter, like in Figure 36. Far from the endpoints and the joints, a steady flow can be described by the Poiseuille solution [66]. In Poiseuille flow, the local velocity is directed exactly against the pressure gradient. The magnitude of the volumetric flow rate, w, can be evaluated by integrating the velocity over a cross-section of the tube orthogonal to its axis. Thus,

$$w = \frac{\pi}{8\mu}\left|\frac{dp}{dx}\right|R^4 \tag{19}$$

where the coordinate x is parallel to the tube axis and R is the radius. Thus,

$$\left|\frac{dp}{dx}\right| = \frac{8\mu q}{\pi}R^{-4} \tag{20}$$

After substitution of this result in Equation (12), one obtains an expression for the rate of condensate dropout in a capillary tube

$$Q_{lc} = \frac{d}{dp}\left(c(p)\varrho_g(p)\right)\frac{8\mu q^2}{\pi R^4} \tag{21}$$

The total flow rates in the narrow and wide tubes are approximately the same. Thus, the rate of condensation in the narrow tube is approximately $\left(\frac{R_1}{R_2}\right)^4$ faster than than in the wider tube. Condensate dropout in the narrow tube only reduces the effective tube diameter, and, therefore, accelerates blocking. The conclusion is that the pore throats get blocked first, and if the throats are much narrower than the pores, the flow will be blocked by accumulation of a very small amount of condensate!

Both examples above involve idealized geometry. The geometry of the flow in natural rocks is much more complex. Figure 30 shows computed pressure distribution inside an image of a tight-sand sample. In larger pores the pressure is almost constant, and the pressure drop happens in narrow passes. Thus, the condensate dropout will more likely block the narrow connections between clusters of larger pores. Such a development will enhance pore-scale compartmentalization of the pore space and may disconnect the gas phase.

The fact that the dropout rate distribution is characterized by the distribution of the scalar product of local velocity and pressure gradient has its impact on upscaling of this distribution to Darcy-scale model. Darcy velocity, $\mathbf{W}$, is volumetric flux. It can be expressed through the mean fluid velocity, $\bar{\mathbf{u}}$:

$$\mathbf{W} = \phi\bar{\mathbf{u}} \tag{22}$$

where ϕ is the medium porosity. By Darcy's law,

$$\mathbf{W} = -\frac{k_g}{\mu_g}\overline{\nabla p} \tag{23}$$

Let us present the velocity and pressure gradient as the sums of mean values and fluctuations, which will be denoted by tilde:

$$\mathbf{u} = \bar{\mathbf{u}} + \widetilde{\mathbf{u}} = -\frac{k_g}{\phi\mu_g}\overline{\nabla p} + \widetilde{\mathbf{u}}, \quad \nabla p = \overline{\nabla p} + \widetilde{\nabla p} \tag{24}$$

The mean values of the fluctuation components are zero. Therefore,

$$\overline{\mathbf{u}\cdot\nabla p} = \bar{\mathbf{u}}\cdot\overline{\nabla p} + \widetilde{\mathbf{u}}\cdot\widetilde{\nabla p} = -\frac{k_g}{\phi\mu_g}\overline{\nabla p}\cdot\overline{\nabla p} + \widetilde{\mathbf{u}}\cdot\widetilde{\nabla p} \tag{25}$$

The last term on the right-hand side evaluates the correlation between local velocity and pressure gradient fluctuations. The Darcy-scale derivation above yielded Equation (8), which neglects the correlation term. In a porous medium modeled by a bundle of capillary tubes, pressure gradient inside of each tube is constant, so the correlation term vanishes. However, in a complex tortuous pore space this term may play a more important role.

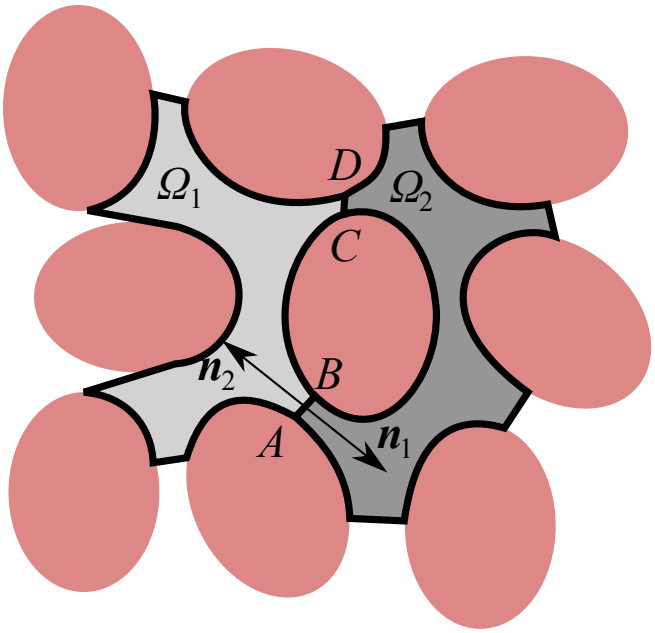

FIGURE 34. The boundaries of domains $\partial\Omega_1$ and $\partial\Omega_2$ are shown as bold lines. After summation, the surface integral components corresponding to the common boundary intervals AB and CD cancel each other since the normal are directed in the opposite directions.

Note that the relationship (12) scales up from the pore scale to Darcy's flow scale. Indeed, since $\nabla \cdot \mathbf{u}_g = 0$, for a domain Ω Green–Gauss–Ostrogradsky divergence theorem [77] yields

$$\int_{\Omega} \nabla p \cdot \mathbf{u}_g \, dV = \int_{\partial\Omega} p\mathbf{u}_g \cdot \mathbf{n} \, dS \tag{26}$$

where $\mathbf{n}$ is the external normal to the surface $\partial\Omega$ bounding domain Ω. The domain should be entirely in the fluid phase. The integrand of the surface integral on the right-hand side of Equation (26) vanishes on the parts of the domain boundary coinciding with the pore walls. This holds true both in case of no-slip flow and in case of slippage, since in both cases the normal component of the velocity at the pore wall is zero. On the common boundary If two non-overlapping domain share part of their boundaries, then the external normal vector for one boundary is an inbound normal vector for the other, and *vice versa*, Figure 34. Therefore, for such domains, the the volume integrals in Equation (26) sum up, but the sum of the surface integral is equal to the surface integral over the boundary of the union of the two domain. Clearly, this additive rule holds true for an arbitrary number of domains.

Now, let us consider small volume in Darcy scale between two equipotential surfaces swept by Darcy's flow field, Figure 35. This domain can be represented as a sum of pore-scale domains, like the ones in Figure 34. According to the summation principle discussed above, the volumetric integral on the left-hand side of Equation (26) is equal to the surface integral of $p\mathbf{u}_f \cdot \mathbf{n}$ evaluated on the surface shown with the bold line in Figure 35. The integrals on the equipotential surfaces $S_1 : p = p_1$ and $S_2 : p = p_2$ yield approximately $-p_1\overline{\mathbf{u}}_g\phi S_1$ and $p_2\overline{\mathbf{u}}_g\phi S_2$, respectively. The mean flow velocities are evaluated on the corresponding equipotential surfaces. The flux through the lateral boundaries is equal to zero because they are formed by the streamlines of the Darcy flow. Therefore, the average fluctuations of the fluid velocities also are equal to zero. Thus, for the domain in Figure 35, one obtains

$$\int_\Omega \nabla p \cdot \mathbf{u}_g \, dV = \int_{S_1 \quad S_2} p\mathbf{w} \cdot \mathbf{n} dS \tag{27}$$

Since Darcy velocity is orthogonal to equipotential surfaces, the integral on the right-hand side of Equation (27) can be extended over the entire boundary of the domain Ω:

$$\int_\Omega \nabla p \cdot \mathbf{u}_g \, dV = \int_{\partial\Omega} p\mathbf{w} \cdot \mathbf{n} dS \tag{28}$$

Applying Green–Gauss–Ostrogradsky theorem to the right-hand side of the last equation, one obtains

$$\int_\Omega \nabla p \cdot \mathbf{u}_g \, dV = \int_\Omega \nabla p \cdot \mathbf{w}_g \, dV \tag{29}$$

The last result implies that the fluctuation term in Equation (25) averages out in passing from pore scale to Darcy flow scale, and Equations (8) and (12) provide two equivalent ways of evaluation of the condensate dropout rate.

Note that local variations of the flow field in a tortuous pore space can be significant. Therefore, local deviations from the average rate can be significant. The impact of tortuosity on the spacial distribution of the condensate dropout rate needs further investigation, which is beyond this study.

The results of this section along with Section 4.1 suggest the following gas-trapping scenario. We assume that water saturation is negligible at the beginning of production. As gas pressure starts depleting in the matrix, condensate drops out. At gas pressure close to unity, the relative permeability to condensate is initially equal to zero. As long as the gas keeps flowing, the condensate accumulates and relative permeability to goes down. The condensate accumulates

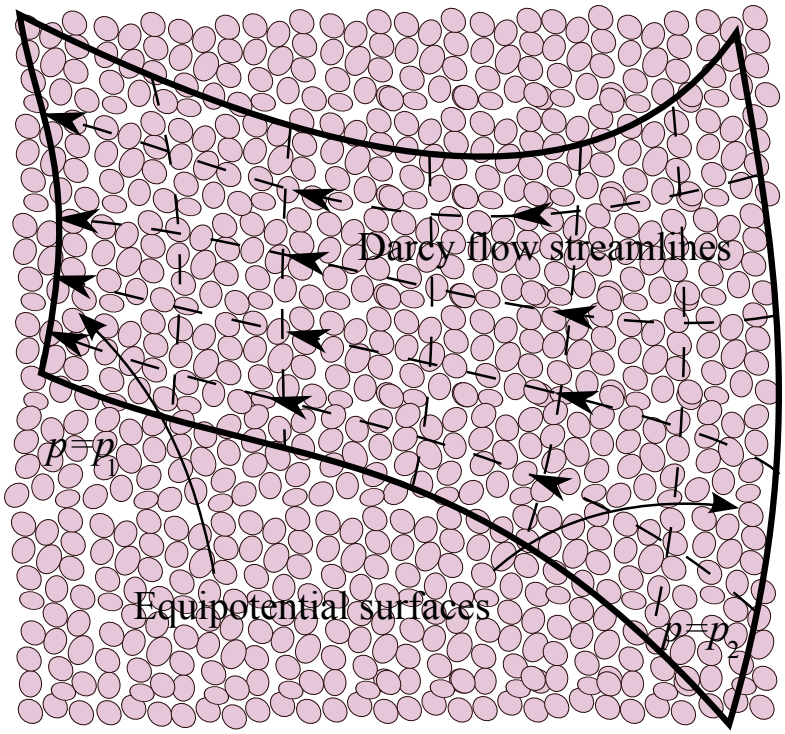

FIGURE 35. A Darcy-scale domain swept by Darcy flow streamlines and bounded between two equipotential surfaces $p = p_1$ and $p = p_2$, $p_2 > p_1$.

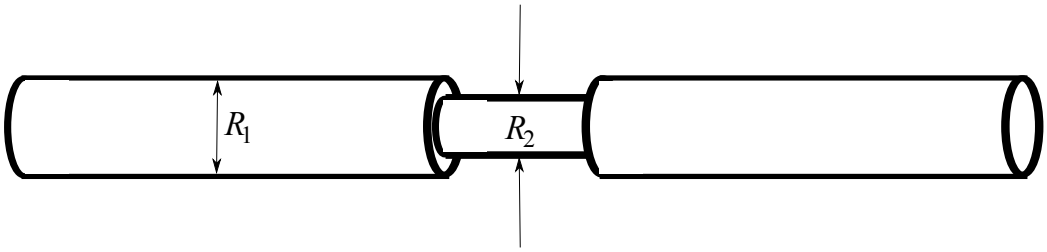

FIGURE 36. Capillary tube with a constriction

faster in the narrow channels, since this is where the pressure gradient is larger. At some point, the condensate saturation will reach a point where gas flow becomes inappreciable. The growing condensate saturation cannot jump over the permeability jail, regardless its size; Indeed, the gas phase becomes immobile before the condensate becomes mobile. Thus, the saturation will stagnate in the permeability jail, even if the latter consists of a single value of saturation. *In-situ* condensate dropout without advective transport is negligible, since the condensate in liquid phase is much denser than in the gas phase. With gas flow, there is an accumulation of condensate over time. Once the permeability jail is reached, no further condensate dropout can appreciable change the condensate saturation.

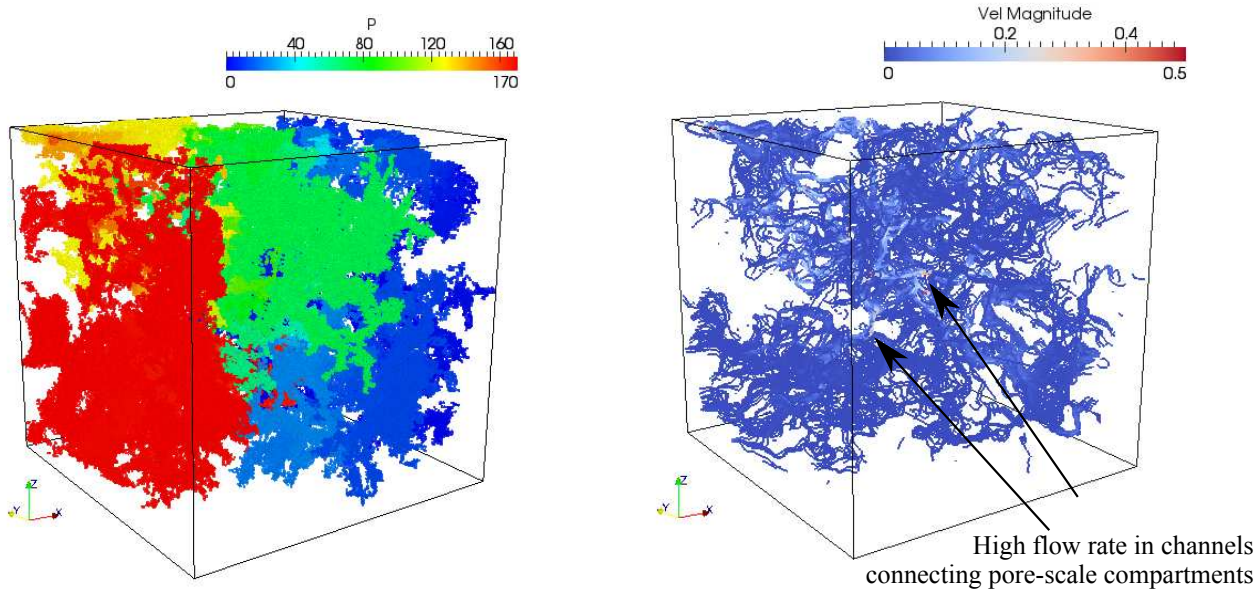

FIGURE 37. Simulated pore-scale pressure distribution, on the left, and flow streamlines, on the right. The compartmentalization effect creates a small number of channels with high flow velocity and pressure gradient.

Figure 37 shows a pressure field and flow streamlines evaluated at about 10 % brine saturation. The flow is in x direction. The dimensionless distribution displayed on the left-hand picture suggests that the entire pore space is broken into a few clusters. Inside each cluster, the pressure is almost constant and the flow is distributed reasonably uniformly between the pores. The clusters are connected *via* small number of flow channels. In these channels, the pressure drop is the highest, and the flow velocity is the highest relative to the neighbors. Equation (12) implies that the highest rate of condensate dropout must occur in these channels. This self-enhancing mechanism can accelerate the flow blockage. Capillarity will redistribute the condensate, and will help to slow down the clogging.

One way to destroy this stagnation and re-mobilize the fluids could be shifting the condensation pressure by changing the temperature. In this approach, the delivery of heat energy may only rely on heat conduction due to the blockage of flow, which is not efficient. An alternative approach could be seismic stimulation of the stagnant zone with a hope that the condensate is near the bubbling point, and pressure fluctuation will force some gas release. The released gas will increase the pore pressure and change the saturation, so some fluid mobilization can be achieved. A small amount of water at the pore walls should create a lubricating effect and

facilitate mobilization of the gas condensate. These considerations are speculative at this point, and require thorough study before trying in the field. Apparently, a good practice would be minimization of the formation damage by retrograde gas condensation through controlling the gas recovery rate. A high rate especially at the early time of production may have an adverse effect on the ultimate recovery.

6. Conclusions

Natural gas in tight-sand reservoirs represents a considerable energy resource. Tight gas sands are spread in a number of on-shore basins. The biggest areas in the United States are a number of basins east of Rocky Mountains in the Mid West, and Appalachian Basin in the East. The contribution of this resource into the United States energy portfolio is large now and is anticipated to remain such in coming decades.

Although tight gas sand is a generic term covering a variety of hydrocarbon-bearing formations, they all are characterized by low permeability of the reservoir rock. Gas production at economically justified rates requires stimulation of the well by hydrofracturing. This defining property of tight sand makes them different from conventional gas resources.

This study has been focused on the pore-scale mechanisms of gas flow and recovery. It relies on evaluation of single- and two-phase flow properties of the rock from analysis of the pore-space geometry.

Different imaging techniques cover different scales and resolution and produce 2D or 3D data. A low-resolution medical scanner was used to detect fractures and analyze other irregularities in the reservoir cores. In most cases, the preferences for selecting subsamples for micron-scale x-ray computed microtomography (micro-CT) at the Advanced Light Source facility tomography beamline 8.3.2 were to avoid the irregularities, so that the sample would have "typical" matrix properties. The selected samples were cut and prepared for micro-CT scanning at the LBNL machine shop. Certainly, high-resolution imaging imposes stricter constraints on the sample size. An optical microscope and Scanning electron microscopy were used for verification of the micro-CT reconstructed images and examination of the subresolution structures, which are present in the micro-CT data but not in definitive details.

In-house custom codes and publicly available libraries were used to analyze the digital data. The Method of Maximal Inscribed Spheres computes capillary-equilibrium fluid distribution

for two-phase flow. Capillary pressure curves have been computed for the samples whose 3D reconstructions show sufficient porosity. Simulation of invasion percolation generates drainage capillary pressure curves, whereas ordinary percolation produces imbibition capillary pressure. Although the approach used in this study focuses on a volume measured in hundreds of microns or millimeters, the obtained results are consistent. We interpret this consistency as the validation of the method and the representativeness of the samples.

Five reservoir samples have been images with different imaging techniques. In some samples, the inter granular void space reduces to slit-like pores. Such features present a difficulty for imaging and can complicate fluid flow modeling and simulations and evaluation of capillary-equilibrium fluid distribution. The images of a number of samples show a variety of pores structures. The grain sizes of the scanned tight-sand samples do not significantly differ from those of conventional sandstones. The striking contrast is in the grain pack density.

A finite-difference flow simulator gas been upgraded to evaluate relative permeability curves from the fluid distributions generated by the Maximal Inscribed Sphere Simulations. The computed curves are in agreement with laboratory data. The number of saturation values is constrained by the resolution of the image. The number of measurements is limited due to the low permeability of the rock and consequent difficulties of conducting steady-flow experiments. Both numbers where less than ten. There is a potential for improvement by increasing the resolution of the images. We believe that voxel size of the order of hundred nanometers would allow for significant improvement of the simulations. Evaluation of the relative permeability curves is the most computationally intense part of simulations. The size of the domain is limited by the available computing power. One of the objectives of this study was to demonstrate that simulation can run on a personal desktop workstation. Optimizing the codes for massive parallel machines may expand the capabilities of the method. There is a potential "embarrassing" parallelization of the computations by evaluating relative permeabilities at different saturations independently.

The following observation have been made.

The drainage capillary pressure curves computed for tight-sand samples show capillary barriers exceeding those evaluated for conventional sandstones. It is an indication of narrow inter-pore connections hindering the invasion of the nonwetting fluid. Simulations show that the saturation connectivity threshold for tight sands is unusually low. If simulations for conventional sandstones show that the nonwetting fluid may stay connected at water saturation near 70%, simulations

on images of tight sand samples show that 30% wetting fluid saturation can make the gas phase disconnected. This observation suggests the capillary nature of gas trapping by water or gas condensate. Computed relative permeability to gas vanishes at saturations near 30%. The water relative permeability curve intersects the gas permeability curve near zero. It means that gas and water flows are mutually exclusive. Gas may be disconnected but still present in the form of bubbles. These bubbles occupy the central parts of the pores leaving narrow passes for the wetting fluid flow. Since water or gas condensate viscosity is much higher than that of gas, the mobility of the wetting fluid is very low except almost full saturations where the water relative permeability approaches one. This observation explains the pore-scale mechanism of the so-called permeability jail reported in the literature: there exists a range of saturations where no fluid flow is possible. The nature of gas flow blocking by water or condensate is capillary, whereas the wetting fluid flow blocking is bot dynamic (low permeability in the pore corners) and capillary (dispersed gas bubbles).

A simple pore-scale model of retrograde gas condensation suggests that the rate of dropout is scaled with the dot product of the pressure gradient and fluid velocity. This model naturally upscales to Darcy-flow scale, where the retrograde condensation rate is proportional to the pressure gradient squared. Simulation of gas flow in a capillary tube of variable cross-section diameter shows that in the narrow parts the condensate dropout rate is higher than that in a wider tube part with the proportionality coefficient equal to the inverse ratio of the radii raised to the fourth degree. Thus, retrograde condensation will promote clogging the narrow pore throats, which will lead to further disconnection and pore-scale compartmentalization of the gas phase. Because of the permeability jail, a small amount of condensate may completely block gas flow. This blocking mechanism, along with compaction and transport of fines makes gas production from a tight-sand reservoir challenging. On the one hand, pressure maintenance slows down the gas condensate dropout and prevents blockage of the flow. On the other hand, the slow down of the gas recovery caused by a lower pressure gradient can make the recovery project economically unsustainable. Determination of the optimal compromise between the production rate and reservoir damage prevention needs a comprehensive study involving modeling along with laboratory and field experiments.

7. Acknowledgments

This work has been performed at Lawrence Berkeley National Laboratory (LBNL) of the U.S. Department of Energy (DOE) under Contract No. DE-AC02-05CH11231. Portions of this work were performed at the Advanced Light Source Facility, LBNL, which is supported by the Office of Science, Office of Basic Energy Sciences, U. S. Department of Energy, under Contract No. DE-AC02-05CH11231. Funding for this project is provided by RPSEA through the Ultra-Deepwater and Unconventional Natural Gas and Other Petroleum Resources program authorized by the U.S. Energy Policy Act of 2005. RPSEA (www.rpsea.org) is a nonprofit corporation whose mission is to provide a stewardship role in ensuring the focused research, development and deployment of safe and environmentally responsible technology that can effectively deliver hydrocarbons from domestic resources to the citizens of the United States. RPSEA, operating as a consortium of premier U.S. energy research universities, industry, and independent research organizations, manages the program under a contract with the U.S. DOE's National Energy Technology Laboratory.

The samples of gas tight sand reservoir rock have been provided by BP and Chevron. In the computations, we used SparsLib++ and IML++, object-oriented iterative linear algebra code libraries [33]. Andrew Mei of LBNL Engineering prepared the samples for microtomography at the ALS. Alastair McDowell of the ALS helped with microtomography imaging. The authors gratefully acknowledge discussions with Joanne Friedrich of BP, Jairam Kamath, Rafael Salazar-Tio, and Josephine Schembre of Chevron, Alexander Zazovsky of Schlumberger. Dr. Liviu Tomutsa of LBNL Earth Sciences Division was the original developer of CT imaging techniques used in this work and contributed with invaluable advice on pore-scale studies of natural rocks in general. Discussions with professor M. Panfilov of University of Nancy, France, and professor G. Barenblatt of University of California, Berkeley, helped to develop the condensate dropout model. The authors thank Dr. Andrea Cortis and Peter Persoff of LBNL who kindly agreed to review the manuscript and provided a number of valuable recommendations. Possible errors and misconceptions in this study are solely the responsibility of the authors.

Appendix A. Creeping flow model

A computed-tomography image is a three-dimensional array of gray-scale voxels. Each voxel is a cubic volume whose size is determined by the image resolution. At each voxel, the intensity

number is evaluated by solving the inverse problem of image reconstruction from a large number of projections [46]. The intensity number represents the average density of the material in a given voxel: the brighter spots correspond to dense matter, and the darkest spots correspond to void space. A number of methods have been developed for pore-scale modeling of flow and two- and multiphase fluid distribution. Pore-network simulations helped to develop useful insights into the mechanisms of flow and fluid displacement in the pores relying on relatively simple computations [3, 4, 9, 10, 14–18, 35, 38–40, 54, 58, 69, 83, 86]. Flow simulations on generic regular networks [38–40, 108] do not necessarily reflect properties of particular rocks. Although advanced algorithms for generating irregular pore networks which would characterize the pore space geometry of a desired particular rocks have been developed [70, 90], this task is challenging and apparently no routine approach is available. Even in a regular network, the geometry of the cross-sections of the throats can produce unexpected results [8]. Lattice-Boltzmann (LB) approach allows for direct simulation of flow and fluid displacement on a segmented digital 3D image [41, 43, 55, 80, 82, 88, 107]. LB simulations are flexible with respect to complexity of the pore space geometry and the scope of physical phenomena that can be incorporated into the model. LB simulations are very suitable for parallel computations. LB method solves for the flow field in the entire connected pore space. However, modeling no-slip or slippage boundary conditions *via* bounce-back may produce some artifacts [31]. It is not easy to incorporate in LB simulations pressure boundary conditions.

Both pore-network and LB approaches include solution of the Stokes equations of incompressible creeping flow. Averaging the local fluid velocity field and correlating it to the pressure gradient should yield the permeability [50, 51]. Within the pore-network approach, the local velocity is evaluated through the Poiseuille flow in the pore throats. Poiseuille solution yields a simple model for a steady flow in a straight channel whose length is much larger that the width. Usually, pore-network modeling models assume, explicitly or implicitly, that this condition is satisfied.

Alternatively, flow simulations can be performed by finite-difference numerical scheme. The pore voxels provide natural discretization of the domain. A number of implementations of the method have been reported in the literature [2, 13, 71, 72, 87, 91, 96]. Here, we employ a staggered marker-and-cell (MAC) grid: the pressures are evaluated in the voxels centers, whereas the velocity vector components are evaluated on the voxel faces. We use a variation of

the method of projections by Chorin [21]. The finite-difference method can rigorously handle a variety of boundary conditions. However, it is computationally intensive, since it requires solving linear systems of equations with many unknown variables. Comparison between LB and finite-difference approaches does not pick an obvious winner [44, 71].

A.1. **Steady flow of incompressible viscous fluid.** We briefly overview the equations of creeping flow of incompressible viscous fluid (Stokes equations) [66]. Consider a volume of fluid V which is small relative to the dimensions of the flow domain. Let ∂V denote the boundary of V. If $v = v(t, \mathbf{r})$ is the velocity of fluid particle at time t and location $\mathbf{r}$ $\mathbf{r} = (x, y, z)$, then surface integral

$$f(V) = \int_{\partial V} \varrho v \cdot n \, ds \tag{A.1}$$

evaluates the total fluid flux through the boundary ∂V. Here ϱ is the fluid density and $n \, ds$ is surface element with an external unit normal vector $\mathbf{n}$. B shrinking V into a point, we obtain

$$\nabla \cdot v = 0 \tag{A.2}$$

The last equations reflects fluid incompressibility in the absence of sinks and sources. The fluid flow is driven by the stresses and body forces acting on the fluid. Therefore, the rate of variation of the total momentum of the fluid inside the volume V is determined by (a) the fluid flow across the boundary ∂V, which brings slower or faster particles in and out the volume V, (b) the stresses acting on the surface ∂V, and (c) the body forces $\mathcal{F}$, like gravity or electrostatic field, acting on the portion of fluid instantaneously locked in volume V. Thus, we get

$$\frac{d}{dt}(\varrho v) = -\int_{\partial V} \varrho v (v \cdot n) \, ds + \int_{\partial V} T n \, ds + \int_V \mathcal{F} \, dV \tag{A.3}$$

where T is the stress tensor. The latter is the sum of pressure, pI, where I is an identity tensor, and viscous stress S resulting from the interaction between layers of fluid mowing with different velocities

$$T = -pI + T_S \tag{A.4}$$

Clearly, viscous stress tensor must depend on the velocity gradient ∇v. This dependence is linear for a newtonian fluid. Note that fluid circulation around an axis at a constant angular velocity is an example of frictionless flow with non-zero velocity gradient. Therefore, the dependence of viscous friction on ∇v needs a more accurate description. Both T_S and ∇v are 3×3 tensors. In general, a linear relationship between two such tensors involves 81 coefficients. However, the

isotropy of the fluid is usually used to justify reduction of the total number of coefficients to two. So the viscosity stress is presented in the form

$$S = \eta \{T_{Si,j}\} + \zeta \nabla \cdot v I \tag{A.5}$$

where

$$T_{Si,j} = \begin{cases} \dfrac{\partial v_i}{\partial x_j} + \dfrac{\partial v_j}{\partial x_i}, & i \neq j \\ 2\dfrac{\partial v_i}{\partial x_i} - \dfrac{2}{3}\nabla \cdot v, & i = j \end{cases} \tag{A.6}$$

is the shear viscosity component. The coefficients η and ζ are, respectively, shear and second viscosity.

The representation of viscous stress in the form (A.5)–(A.6) can be performed in a slightly different way. The shear stress is a linear function of velocity gradient (or Jacobian) ∇v. This gradient itself is a second-order tensor, which can be represented as the sum of symmetric and anti-symmetric tensors. The anti-symmetric term is dropped because the rotations are irrelevant for viscose friction. The symmetric component of the tensor consists of the elements

$$\frac{1}{2}\left(\frac{\partial v_i}{\partial x_j} + \frac{\partial v_j}{\partial x_i}\right)$$

By subtracting form the diagonal the trace of the symmetrized tensor divided by the dimension, we would obtain (A.5)–(A.6) with a coefficient equal to 0.5. This correction coefficient is traditionally incorporated into the coefficients of viscosity. The last term in Equation (A.5) involving the second viscosity, as well as the divergence term in Equation (A.6), are dropped in our calculations due to the incompressibility of the fluid, Eq. (A.2).

Substitution of equations (A.5)–(A.6) into Eq. (A.3) and passing to the limit as the domain V shrinks into a point results in Navier-Stokes equations for flow of viscous incompressible fluid

$$\frac{\partial}{\partial t} v + (v \cdot \nabla) v = -\frac{1}{\varrho}\nabla p + \nu \nabla^2 v + \mathcal{F} \tag{A.7}$$

where $\nu = \eta/\varrho$ is the kinematic viscosity coefficient. In steady-state flow, the time derivative vanishes:

$$(v \cdot \nabla) v = -\frac{1}{\varrho}\nabla p + \nu \nabla^2 v + \mathcal{F} \tag{A.8}$$

The last equation is further simplified by neglecting the body forces and by the creeping flow assumption. The latter means that the flow velocities are sufficiently small, so that the nonlinear

with respect to v term on the left-hand side can be neglected. Thus, we arrive at steady-state Stokes equations

$$\eta \nabla^2 v = \nabla p \tag{A.9}$$

which must be solved together with the continuity equation (A.2).

To evaluate the Darcy velocity, the sum of fluxes over the pore voxels must be divided by the total area of the sample face. Darcy's law written down for the three pressure gradients

$$\nabla p = \begin{pmatrix} 1 \\ 0 \\ 0 \end{pmatrix}, \begin{pmatrix} 0 \\ 1 \\ 0 \end{pmatrix}, \begin{pmatrix} 0 \\ 0 \\ 1 \end{pmatrix} \tag{A.10}$$

yields the following expression for the permeability tensor:

$$\underline{\underline{K}} = \eta \underline{\underline{\nabla p}}^{-1} \underline{\underline{W}} \tag{A.11}$$

where $\underline{\underline{\nabla p}}$ and $\underline{\underline{W}}$ are tensors constructed from the three pressure gradients and the respective three computed Darcy velocities.

Appendix B. Scaling the permeability and velocity field

We skip the details of the numerical scheme, which will be described elsewhere. Here we just briefly describe how to scale the dimensionless numerical results in order to evaluate permeability in physically meaningful units.

Let us define dimensionless variables in Stokes equations, Equation (A.9), in the following way:

$$\mathbf{v} = v_0 \mathbf{V}, \quad x = DX,\ y = DY,\ z = DZ, \ \text{ and } p = p_0 P \tag{B.1}$$

Then, Equation (A.9) takes on the following dimensionless form:

$$\nabla P = \eta_0 \nabla^2 \mathbf{V} \tag{B.2}$$

where

$$\eta_0 = \frac{\eta v_0}{p_0 D} \tag{B.3}$$

The incompressibility equation, Equation (A.2), remains unchanged in the dimensionless form.

Let D be equal to the voxel size. In simulations, the quantity η_0 is an adjustable computational parameter. Its value is selected to provide for convergence and stability of the iterative scheme.

The pressure scaling factor, p_0, must be selected in a way that the viscosity factor η has a physically meaningful magnitude. The converting factor for velocity is:

$$v_0 = \frac{p_0 \eta_0}{\eta} D = \frac{p_0 \eta_0}{D\eta} D^2 \tag{B.4}$$

After expressing η from Equation (B.3) and taking into account Equations (A.10) and (B.4) one obtains that

$$\underline{\underline{K}} = \frac{\eta_0 p_0 D}{v_0} \frac{D}{p_0} v_0 = D^2 \eta_0 \underline{\underline{W_0}} \tag{B.5}$$

where $\underline{\underline{W_0}}$ is the Darcy velocity evaluated in the units of the discretized system. Thus, to evaluate in physical units a column of the permeability tensor corresponding to one of the columns in Equation (A.10), it suffices to multiply the computed dimensionless vector of Darcy velocity, W_0, by the dimensionless viscosity η_0 and by the physical voxels size squared.

Let voxel size, D, be equal to $D = 5$ μm. To simulate flow corresponding to 1% hydrostatic gradient, which is equal to $1000 \times 9.8 \times 10^{-2}$ Pa/meter, one has to run simulations with the pressure drop by one unit per, one has to put:

$$p_0 = 5 \times 10^{-6}\text{m} \times 1000 \frac{\text{kg}}{\text{m}^3} \times 9.8 \frac{\text{m}}{\text{s}^2} \times 10^{-2}\text{m}/1\text{m} = 4.9 \times 10^{-6} \text{ Pa} \tag{B.6}$$

From Equation (B.4), the Darcy velocity in physical units can be obtained from the dimensionless one by applying a factor of $\frac{\eta_0 p_0 D}{v_0}$.

References

1. Anahita Abadpour and Mikhail Panfilov, *Asymptotic decomposed model of two-phase compositional flow in porous media: Analytical front tracking method for Riemann problem*, Transport in Porous Media **82** (2010), 547–565, 10.1007/s11242-009-9428-8.
2. P. M. Adler, *Fractal porous media III: Transversal Stokes flow through random and Sierpinski carpets*, Transport in Porous Media **3** (1988), no. 2, 185–198.
3. ———, *Porous media, geometry and transports*, Butterworth-Heinemann Series in Chemical Engineering, Butterworth-Heinemann, Boston, 1992.
4. A. Al-Futaisi and T. W. Patzek, *Impact of wettability on two-phase flow characteristics of sedimentary rock: Quasi-static model*, Water Resources Research **39** (2003), no. 2, 1042–1055.

5. Gus Alvarado, J. L. Le Blanc, and F. Farshad, *A new and improved material balance equation for retrograde gas condensate reservoirs – Part I. spe paper 24355*, SPE Rocky Mountain Regional Meeting, 18-21 May 1992, Casper, Wyoming, 1992.
6. W. G. Anderson, *Wettability literature survey– Part 4: Effects of wettability on capillary pressure*, Journal of Petroleum Technology **39** (1987), no. 10, 1283–1300.
7. F. M. Auzerais, J. Dunsmuir, B. B. Ferreol, N. Martys, J. Olson, T. S. Ramakrishnan, D. H. Rothman, and L. M. Schwartz, *Transport in sandstone: A study based on three dimensional microtomography*, Geophysycal Research Letters **23** (1996), 705–708.
8. F. G. Avkhadiev and Anvar R. Kacimov, *Analytical solutions and estimates for microlevel flows*, Journal of Porous Media **8** (2005), no. 2, 125–148.
9. S. Bakke and P. E. Øren, *3-D pore-scale modelling of heterogeneous sandstone reservoir rocks and quantitative analysis of the architecture, geometry and spacial continuity of the pore network. spe 35479*, European 3-D Reservoir Modelling Conference (Stavanger, Norway), SPE, 1996, pp. 35–45.
10. Stig Bakke and Pål-Eric Øren, *3-D pore-scale modelling of sandstones and flow simulations in the pore networks*, SPE Journal **2** (1997), 136–149.
11. G. I. Barenblatt, I. P. Zheltov, and I. N. Kochina, *Basic concepts in the theory of seepage of homogeneous liquids in fissured rocks*, Applied Mathematics and Mechanics **24** (1960), no. 5, 1286–1303.
12. D. B. Bennion, F. B. Thomas, and B. Schulmeister, *Retrograde condensate dropout phenomena in rich gas reservoirs-impact on recoverable reserves, permeability, diagnosis, and stimulation techniques*, Journal of Canadian Petroleum Technology **40** (2001), no. 12, 5–8.
13. Dominique Bernard, yvind Nielsen, Luc Salvo, and Peter Cloetens, *Permeability assessment by 3D interdendritic flow simulations on microtomography mappings of Al-Cu alloys*, Materials Science and Engineering: A **392** (2005), no. 1-2, 112–120.
14. M. J. Blunt, *Flow in porous media - pore-network models and multiphase flow*, Current Opinion in Colloid & Interface science **6** (2001), no. 3, 197–207.
15. M. J. Blunt and P. King, *Relative permeabilities from two- and three-dimensional pore-scale metwork modeling*, Transport in Porous Media **6** (1991), 407–433.
16. Martin Blunt and Peter King, *Macroscopic parameters from simulations of pore scale flow*, Physical Review A **42** (1990), no. 8, 4780–4787.

17. Steven Bryant and Martin Blunt, *Prediction of relative permeability in simple porous-media*, Physical Review A **46** (1992), 2004–2011.
18. Steven L. Bryant, Peter R. King, and David W. Mellor, *Network model evaluation of permeability and spatial correlation in a real random sphere packing*, Transport in Porous Media **11** (1993), 53–70.
19. P. C. Carman, *Fluid flow through a granular bed*, Trans. Inst. Chem. Eng. London **15** (1937), 150–156.
20. J. H. P. Castelijns and J. Hagoort, *Recovery of retrograde condensate from naturally fractured gas-condensate reservoirs*, SPE Journal **24** (1984), 707–717.
21. A. J. Chorin, *Numerical solution of the Navier–Stokes equations*, Math. Comp. **22** (1968), 745–762.
22. P. Chowdlah, *Influence of water-desaturation technique and stress on laboratory measurement of hydraulic properties of tight sandstones*, SPE Formation Evaluation **3** (1988), no. 4, 679–685.
23. Robert M. Cluff and Alan P. Byrnes, *Relative permeability in tight gas sandstone reservoirs – the "Permeability Jail" model*, SPWLA 51st Annual Logging Symposium, June 19-23, 2010.
24. M. E. Coles, R. D. Hazlett, E. L. Muegge, K. W. Jones, B. Andrews, Dowd, P. Siddons, and A. Peskin, *Developments in synchrotron X-ray microtomography with applications to flow in porous media*, SPE Reservoir Evaluation and Engineering **1** (1998), no. 4, 288–296.
25. M. E. Coles, R. D. Hazlett, P. Spanne, E. L. Muegge, and M. J. Furr, *Characterization of reservoir core using computed microtomography*, SPE Journal **1** (1996), no. 3, 295–302.
26. M. E. Coles, R. D. Hazlett, P. Spanne, W. E. Soll, E. L. Muegge, and K. W. Jones, *Pore level imaging of fluid transport using synchrotron X-ray microtomography*, Journal of Petroleum Science and Engineering **19** (1998), 55–63.
27. J. T. Comisky, K. E. Newsham, J. A. Rushing, and T. A. Blasingame, *A comparative study of capillary-pressure-based empirical models for estimating absolute permeability in tight gas sands*, SPE Annual Technical Conference and Exhibition, 11-14 November 2007, Anaheim, California, U.S.A., 2007.
28. Richard A. Dawe and Carlos A. Grattoni, *Fluid flow behaviour of gas-condensate and near-miscible fluids at the pore scale*, Journal of Petroleum Science and Engineering **55** (2007),

no. 3-4, 228 – 236.

29. P.-G. de Gennes, *Wetting: statics and dynamics*, Reviewes of Modern Physics **57** (1985), no. 3, 827–863.
30. B. V. Derjagin, N. V. Churaev, and V. M. Muller, *Surface forces*, Plenum Press, New York, 1987.
31. Dominique d'Humières and Irina Ginzburg, *Viscosity independent numerical errors for Lattice Boltzmann models: From recurrence equations to "magic" collision numbers*, Computers & Mathematics with Applications **58** (2009), no. 5, 823–840.
32. M. Dierick, B. Masschaele, and L. Van Hoorebeke, *Octopus, a fast and user-friendly tomographic reconstruction package developed in LabView®*, Measurement Science and Technology **15** (2004), 1366–1370.
33. Jack Dongarra, Andrew Lumsdaine, Xinhiu Niu, Pozo Roldan, and Karin Remington, *A sparse matrix library in C++ for high performance architectures*, Proceedings of the Second Object Oriented Numerics Conference, 1994.
34. P. Duhem, *On the liquefaction of a mixture of two gases. composition of the liquid and the vapor*, The Journal of Physical Chemistry **5** (1901), no. 2, 91–112.
35. V. M. Entov, *The micromechanics of flow in porous media*, Fluid Dynamics **27** (1992), no. 6, 824–833.
36. T. Ertekin and L. Ayala, *Numerical analysis of retrograde gas behavior in fissured systems: The single-block model*, Petroleum Science and Technology **26** (2008), no. 10, 1141–1160.
37. Li Fan, Billy W. Harris, A. Jamaluddin, Jairam Kamath, Robert Mott, Gary A. Pope, Alexander Shandrygin, and Curtis Hays Whitson, *Understanding gas-condensate reservoirs*, Oilfield Review (2005), 14–27.
38. I. Fatt, *The network model of porous media. 1. Capillary pressure characteristics*, Trans. AIME **207** (1956), no. 7, 144–159.
39. _____, *The network model of porous media. 2. Dynamic properties of a single size tube network*, Trans. AIME **207** (1956), no. 7, 160–163.
40. _____, *The network model of porous media. 3. Dynamic propertries of networks with tube radius distribution*, Trans. AIME **207** (1956), no. 7, 164–181.
41. J. T. Fredrich, A. A. DiGiovanni, and D. R. Noble, *Predicting macroscopic transport properties using microscopic image data*, Journal of Geophysical Research **111** (2006), B03201.

42. Boyun Guo, Ali Ghalambor, and Shengkai Duan, *Correlation between sandstone permeability and capillary pressure curves*, Journal of Petroleum Science and Engineering **43** (2004), no. 3-4, 239 – 246.

43. Jens Harting, Maddalena Venturoli, and Peter V. Coveney, *Large-scale grid-enabled lattice Boltzmann simulations of complex fluid flow in porous media and under shear*, Philosophical Transactions of the Royal Society A **362** (2004), 1703–1722.

44. Xiaoyi He, Gary D. Doolen, and T. Clark, *Comparison of the Lattice Boltzmann method and the artificial compressibility method for Navier-Stokes equations*, Journal of Computational Physics **179** (2002), no. 2, 439–451.

45. Nélio Henderson, Juan C. Brêtta, and Wagner F. Sacco, *A three-parameter Kozeny-Carman generalized equation for fractal porous media*, Chemical Engineering Science **65** (2010), no. 15, 4432 – 4442.

46. Gabor T. Herman, *Image reconstruction from projections: The fundamentals of computerized tomography*, Academic Press, New York, 1980.

47. R. Hilfer and F. Doster, *Percolation as a basic concept for macroscopic capillarity*, Transport in Porous Media **82** (2010), no. 3, 507–519.

48. G. J. Hirasaki, *Wettability: Fundamentals and surface forces*, SPE Formation Evaluation **6** (1991), 217–226.

49. S. A. Holditch, *Tight gas sands*, Journal of Petroleum Technology (2006), 86–94.

50. M. King Hubbert, *The theory of ground-water motion*, Journal of Geology **48** (1940), 785–943.

51. ———, *Darcy's law and the field equations of the flow of underground fluids*, Trans. AIME **207** (1956), no. 7, 222–239.

52. Pavel Iassonov, Thomas Gebrenegus, and Markus Tuller, *Segmentation of X-ray computed tomography images of porous materials: A crucial step for characterization and quantitative analysis of pore structures*, Water Resour. Res. **45** (2009), no. 9, W09415–.

53. Jacob N. Israelachvili, *Intermolecular and surface forces*, 2 ed., Academic Press, New York, N. Y, 1992.

54. L. Jia, C. M. Ross, and A. R. Kovscek, *A pore-network-modeling approach to predict petrophysical properties of diatomaceous reservoir rock*, SPE Reservoir Evaluation & Engineering **10** (2006), no. 6, 597–608.

55. G. Jin, T.W. Patzek, and D. B. Silin, *Direct prediction of the absolute permeability of unconsolidated and consolidated reservoir rock. SPE 90084*, 2003 SPE Annual Technical Conference and Exhibition (Houston, Texas, U.S.A.), SPE, 2004.

56. Donald L. Katz and Frederick Kurata, *Retrograde condensation*, Industrial & Engineering Chemistry **32** (1940), no. 6, 817–827.

57. J. H. Kinney and M. C. Nichols, *X-ray tomographic microscopy (xtm) using synchrotron radiation*, Annual Review of Materials Science **22** (1992), no. 1, 121–152.

58. Mark A. Knackstedt, Adrian P. Sheppard, and Muhammad Sahimi, *Pore network modelling of two-phase flow in porous rock: the effect of correlated heterogeneity*, Advances in Water Resources **24** (2001), 257–277.

59. G. Kowalski, *Suppression of ring artifacts in fan-beam scanners*, Journal of Computer Assisted Tomography **1** (1977), no. 2, 266.

60. J. Kozeny, *Über kapillare Leitung des Wassers im Boden*, Sitzungsberichte Wiener Akademie **136** (1927), no. 2a, 271–306.

61. M. Krause, J.-C. Perrin, and S. M. Benson, *Modeling permeability distributions in a sandstone core for history matching coreflood experiments SPE paper 126340*, SPE International Conference on CO_2 Capture, Storage, and Utilization, 2-4 November 2009, San Diego, California, USA, 2009.

62. M. Kumar, T. J. Senden, M. A. Knackstedt, S. Latham, W. V. Pinczewski, R. M. Sok, A. Sheppard, and M. L. Turner, *Imaging of core scale distribution of fluids and wettability*, International Symposium of the Society of Core Analysts (Abu Dhabi, UAE.), 2008.

63. Keith A. Kvenvolden, *Methane hydrate – a major reservoir of carbon in the shallow geosphere?*, Chemical Geology **71** (1988), no. 1-3, 41 – 51, Origins of Methane in the Earth.

64. Keith A. Kvenvolden, *Potential effects of gas hydrate on human welfare*, Proc Natl Acad Sci U S A **96** (1999), no. 7, 3420–3426.

65. Jean Laherrere, *Oceanic hydrates: more questions than answers*, Energy, Exploration & Exploitation **18** (2000), no. 4, 349–383.

66. L. D. Landau and E. M. Lifshitz, *Course of theoretical physics. Fluid Mechanics*, Series in advanced physics, vol. 6, Addison-Wesley, Reading, Mass., 1959.

67. B. E. Law and W. W. Dickinson, *Conceptual model for origin of abnormally pressured gas accumulations in low-permeability reservoirs*, AAPG Bulletin **69** (1985), no. 8, 1295–1304.

68. M. C. Leverett, W. B. Lewis, and M. E. True, *Dimensional-model studies of oil-field behavior*, Trans. AIME **146** (1942), 175–193.

69. W. B. Lindquist, *Network flow model studies and 3D pore structure*, Fluid Flow and Transport in Porous Media: Mathematical and Numerical Treatment (Z. Chen and R. E. Ewing, eds.), Contemporary Mathematics, vol. 295, American Mathematical Society, 2002.

70. W. B. Lindquist and A. Venkatarangan, *Investigating 3D geometry of porous media from high resolution images*, Phys. Chem. Earth (A) **25** (1999), no. 7, 593–599.

71. C. Manwart, U. Aaltosalmi, A. Koponen, R. Hilfer, and J. Timonen, *Lattice-Boltzmann and finite-difference simulations for the three-dimensional porous media*, Physical Review E **66** (2002), 016702 1–11.

72. C. Manwart and R. Hilfer, *Numetrical simulations of creeping fluid flow in reconstruction models of porous media*, Physica A **314** (2002), 706–713.

73. W. D. McCain and R. A. Alexander, *Sampling gas-condensate wells*, SPE Reservoir Engineering **7** (1992), no. 3, 358–362.

74. Alexei V. Milkov, *Global estimates of hydrate-bound gas in marine sediments: how much is really out there?*, Earth-Science Reviews **66** (2004), no. 3-4, 183–197.

75. George J. Moridis and E. Dendy Sloan, *Gas production potential of disperse low-saturation hydrate accumulations in oceanic sediments*, Energy Conversion and Management **48** (2007), no. 6, 1834–1849.

76. Siyavash Motealleh and Steven L. Bryant, *Quantitative mechanism for permeability reduction by small water saturation in tight-gas sandstones*, SPE Journal **14** (2009), no. 2, 252–258.

77. M. Evans Munroe, *Modern multidimensional calculus*, Addison-Wesley, 1963.

78. G. C. Naik, *Tight gas reservoirs — an unconventional natural energy source for the future*, Tech. report, 2003.

79. K.E. Newsham and J.A. Rushing, *Laboratory and field observations of an apparent sub capillary-equilibrium water saturation distribution in a tight gas sand reservoir SPE 75710*, 2002 SPE Gas Technology Symposium held in Calgary, Alberta Canada, 30 April2 May, SPE, 2002.

80. David R. Noble, Shiyi Chen, John G. Georgiadis, and Richard O. Buckius, *A consistent hydrodynamic boundary condition for the lattice Boltzmann method*, Physics of Fluids **7**

(1995), no. 1, 203–209.

81. Myeong Noh and Abbas Firoozabadi, *Wettability alteration in gas-condensate reservoirs to mitigate well deliverability loss by water blocking*, SPE Reservoir Evaluation and Engineering **11** (2008), no. 4, 676–685.
82. R. M. O'Connor and J. T. Fredrich, *Microscale flow modelling in geologic materials*, Physics and Chemistry of the Earth, Part A: Solid Earth and Geodesy **24** (1999), no. 7, 611–616.
83. P. E. Øren, S. Bakke, and O. J. Arntzen, *Extending predictive capabilities to network models*, SPE Journal **3** (1998), 324–336.
84. M. Panfilov and N. Shilovich, *Flow of fluids with substantially different mobilities through a porous medium in the presence of phase transitions: Boundary layer phenomena, spatial phase structures, and instability of the flow*, Fluid Dynamics **35** (2000), 258–267, 10.1007/BF02831434.
85. I. Panfilova and M. Panfilov, *Near-critical gasliquid flow in porous media: Monovariant model, analytical solutions and convective mass exchange effects*, Transport in Porous Media **56** (2004), 61–85, 10.1023/B:TIPM.0000018391.55013.22.
86. T. W. Patzek, *Verification of a complete pore network simulator of drainage and imbibition*, SPE Journal **6** (2001), no. 2, 144–156.
87. M. Piller, G. Schena, M. Nolich, S. Favretto, F. Radaelli, and E. Rossi, *Analysis of hydraulic permeability in porous media: From high resolution x-ray tomography to direct numerical simulation*, Transport in Porous Media **80** (2009), 57–78, 10.1007/s11242-009-9338-9.
88. M. Prodanovic, W. B. Lindquist, and R. S. Seright, *3D image-based characterization of fluid displacement in a Berea core*, Advances in Water Resources **30** (2007), 214–226.
89. R. Quong, *Permeability of Fort Union formation sand stone samples: project Rio Blanco*, Tech. report, Lawrence Livermore Laboratory, 1973.
90. Gianni Schena and Stefano Favretto, *Pore space network characterization with sub-voxel definition*, Transport in Porous Media **70** (2007), 181–190, 10.1007/s11242-006-9094-z.
91. L. M. Schwartz, N. Martys, D. P. Bentz, E. J. Garboczi, and S. Torquato, *Cross-property relations and permeability estimation in model porous media*, Physical Review E **48** (1993), no. 6, 4584 – 4591.
92. Mehmet Sezgin and Bülent Sankur, *Survey over image thresholding techniques and quantitative performance evaluation*, J. Electron. Imaging **13** (2004), 146–165.

93. Keith W. Shanley, Robert M. Cluff, and John W. Robinson, *Factors controlling prolific gas production from low-permeability sandstone reservoirs: Implications for resource assessment, prospect development, and risk analysis*, AAPG Bulletin **88** (2004), no. 8, 1083–1121.

94. Polad M Shikhaliev, *Beam hardening artefacts in computed tomography with photon counting, charge integrating and energy weighting detectors: a simulation study*, 2005, pp. 5813–.

95. D. Silin and T. Patzek, *Pore space morphology analysis using maximal inscribed spheres*, Physica A. Statistical Mechanics and its Applications **371** (2006), 336–360.

96. D. B. . Silin and T. W. Patzek, *Predicting relative-permeability curves directly from rock images. SPE 124974*, 2009 SPE Annual Technical Conference and Exhibition (New Orleans, Louisiana, U.S.A.), SPE, 2009.

97. Dmitriy Silin, Liviu Tomutsa, Sally Benson, and Tad Patzek, *Microtomography and pore-scale modeling of two-phase fluid distribution*, Transport in Porous Media (2010), 1–21, 10.1007/s11242-010-9636-2.

98. Dmitry B. Silin, Guodong Jin, and Tad W. Patzek, *Robust deteremination of the pore-space morphology in sedimentary rocks*, Journal of Petroleum Technology (2004), 69–70.

99. P. Spanne, J. F. Thovert, C. J. Jacquin, W. B. Lindquist, K. W. Jones, and P. M. Adler, *Synchrotron Computed Microtomography of Porous Media: Topology and Transports*, Phys. Rev. Lett. **73** (1994), no. 14, 2001–2004.

100. A. H. Thompson and R. A. Raschke, *Estimation of absolute permeability from capillary pressure measurements*, SPE Annual Technical Conference and Exhibition, 27-30 September 1987, Dallas, Texas, 1987.

101. Liviu Tomutsa, Dmitriy Silin, and Velimir Radmilovic, *Analysis of chalk petrophysical properties by means of submicron-scale pore imaging and modeling*, SPE Reservoir Evaluation and Engineering **10** (2007), no. 3, 285–293.

102. T. D. van Golf-Racht, *Fundamentals of fractured reservoir engineering*, Elsevier Scinetific Publishing Company, Amsterdam, 1982.

103. Matthew R. Walsh, Steve H. Hancock, Scott J. Wilson, Shirish L. Patil, George J. Moridis, Ray Boswell, Timothy S. Collett, Carolyn A. Koh, and E. Dendy Sloan, *Preliminary report on the commercial viability of gas production from natural gas hydrates*, Energy Economics **31** (2009), no. 5, 815–823.

104. Jill S. Ward and Norman R. Morrow, *Capillary pressure and gas relative permeabilities of low-permeability sandston*, SPE Formation Evaluation **2** (1987), 345–356.

105. J. E. Warren and P. J. Root, *The behavior of naturally fractured reservoirs*, SPEJ (1963), 245–255.

106. J. D. Wells and J. O. Amaefule, *Capillary pressure and permeability relationships in tight gas sands*, SPE/DOE Low Permeability Gas Reservoirs Symposium, 19-22 March 1985, Denver, Colorado, 1985.

107. Ronaldo I. White, Joshua A. Borja and Joanne T. Fredrich, *Calculating the effective permeability of sandstone with multiscale lattice Boltzmann/finite element simulations*, Acta Geotechnica **1** (2006), 195–209.

108. B. Xu, J. Kamath, Y. C. Yortsos, and S. H. Lee, *Use of pore-network models to simulate laboratory corefloods in a heterogeneous carbonate sample*, SPE Journal **4** (1999), no. 4, 179–185.

Lawrence Berkeley National Laboratory, 1 Cyclotron Road, MS 90-1116, Berkeley, CA 94720, USA